An Investigation of Convection behind the Cape Canaveral Sea-Breeze Front

P. ANIL RAO* AND HENRY E. FUELBERG

Department of Meteorology, The Florida State University, Tallahassee, Florida

(Manuscript received 29 March 1999, in final form 10 February 2000)

ABSTRACT

A three-dimensional numerical simulation of land–water circulations near Cape Canaveral, Florida, is performed using the Advanced Regional Prediction System. The role of Kelvin–Helmholtz instability (KHI) in determining the time and location of convection behind the sea-breeze front is examined. The model configuration attempts to improve upon limitations of previous work (e.g., resolution, surface characteristics, initial state). It provides a detailed and realistic simulation of the desired features.

The simulation exhibits a single precipitating storm that forms behind the sea-breeze front. This postfrontal storm develops when an outflow boundary intersects a deep layer of upward motion above the marine air. The region of ascent initially is the remnant of a cell that formed along the sea-breeze front, but before the cell decays, a portion of its upward motion is intensified and displaced. The modification of the ascent is a product of KHI that is occurring on top of the sea-breeze interface in the form of billows. The region of enhanced ascent then moves backward with the billow until the outflow boundary arrives. Thus, KHI can be critical in determining the location and time of storm development that occurs behind the Cape Canaveral sea-breeze front.

1. Introduction

The sea breeze is a direct circulation that occurs during the summer months in many coastal regions. It is a product of temperature differences between the land and ocean, consisting of onshore flow during the day (sea breeze) and offshore flow at night (land breeze). Details about characteristics of the sea breeze can be found in Simpson (1994).

The leading edge of the advancing cool, moist sea air, called the sea-breeze front, is a region of low-level convergence that sometimes produces deep convection. Although this frontal convection is well documented (e.g., Nicholls et al. 1991; Pielke et al. 1991; Blanchard and Lopez 1985; Burpee 1984), much less is known about convection that sometimes occurs *behind* the sea-breeze front in the comparatively stable air. This research investigates possible mechanisms for post-sea-breeze convection.

Sea-breeze circulations have been studied extensively during the past several decades (e.g., Byers and Rodebush 1948; Neumann 1951; Estoque 1962; Walsh 1974; Mahrer and Segal 1985; Wakimoto and Atkins 1994). Observational studies have shown that sea-breeze characteristics are directly related to the prevailing wind speed and direction (Nicholls et al. 1991). For example, the synoptic flow over Florida has been categorized into four ''types'' (Blanchard and Lopez 1985), each producing different degrees of inland penetration and sea-breeze intensity. In addition, offshore synoptic flow increases the likelihood of deep convection due to increased surface convergence. Factors such as the horizontal temperature gradient across the front also influence inland penetration and convective potential (Simpson et al. 1977).

Studies using numerical models (e.g., Zhong and Takle 1993; Mahrer and Segal 1985; Pielke 1974; Neumann and Mahrer 1971) have reproduced many of the results discussed above. For example, Estoque (1962) used a two-dimensional (2D) hydrostatic model to investigate the effect of the prevailing winds on the sea breeze. His results were consistent with those of Blanchard and Lopez (1985); for example, offshore prevailing wind produces enhanced vertical motion along the sea-breeze front. While some of Estoque's assumptions (e.g., hydrostatic atmosphere, no radiation or latent heat release, 2D) were quite restrictive, more recent and more sophisticated (i.e., nonhydrostatic) numerical models (e.g., Nicholls et al. 1991; Xian and Pielke 1991; Arritt 1993) have confirmed many of his conclusions. Zhong et al. (1991) used a hydrostatic 3D mesoscale model at 3-km horizontal resolution to examine inter-

* Current affiliation: Universities Space Research Association, NASA Goddard Space Flight Center, Greenbelt, Maryland.

Corresponding author address: Dr. P. Anil Rao, Universities Space Research Association, NASA Goddard Space Flight Center, Mesoscale Atmospheric Processes Branch, Code 912, Greenbelt, MD 20771.
E-mail: rao@gilbert.gsfc.nasa.gov

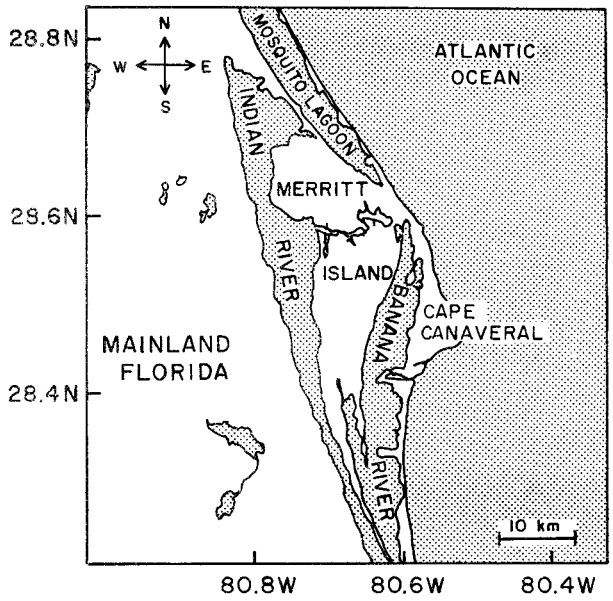

FIG. 1. Physiography near Cape Canaveral, FL.

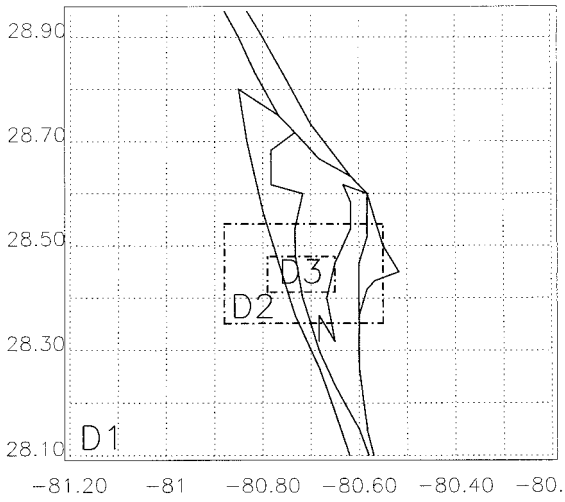

FIG. 2. Locations of the three grid domains utilized for numerical simulation. Grids D1, D2, and D3 contain horizontal resolutions of 1.6 km, 400 m, and 100 m, respectively.

actions between the sea breeze and river breezes found over the Cape Canaveral area of Florida. Their numerical model successfully simulated the onset time and inland movement of the sea breeze and Indian River convergence zones. They found that the Indian River was very important because it created a river breeze with large vertical motions.

The inland-moving sea-breeze front can interact with other boundary layer circulations that occur over the heated land surface. One such feature is horizontal convective rolls (HCRs). HCRs typically form over the heated land surface when some vertical wind shear is present. They are counterrotating pairs of helices oriented horizontally within the convective boundary layer that tend to align parallel to the mean flow (Asai and Naksuji 1973). Interactions between the sea breeze and HCRs have been investigated both observationally (e.g., Atkins et al. 1995; Weckwerth et al. 1996, 1997) and by numerical modeling (e.g., Rao et al. 1999; Dailey and Fovell 1999; Weckwerth et al. 1997). The HCRs were shown to create preferred regions for convective development along the sea-breeze front due to the combination of their two sources of upward motion.

An even smaller scale circulation, Kelvin–Helmholtz instability (KHI), can interact with density currents (e.g., sea and river breezes, outflow boundaries). KHI occurs in areas of enhanced velocity shear and/or a local minimum of static stability in the mean flow. It contributes strongly to the dissipation of larger-scale motions into turbulence. Taylor (1931) noted that a Richardson number (Ri) less than 0.25 is a necessary condition for the onset of KHI.

KHI often is observed in the atmosphere as vortices or billows (KHBs). KHBs form at the leading edge (head) of the density current, grow in amplitude, and then dissipate as they propagate backward relative to the front (e.g., Simpson 1969; Droegemeier and Wilhelmson 1987; Nielsen 1992). The size and structure of KHBs depend on the initial Ri of the flow, with larger billows typically producing the greatest vertical velocities. Laboratory experiments have indicated that these vertical motions can reach 5 m s^{-1} (Browning 1971). Weckwerth and Wakimoto (1992), who studied a thunderstorm outflow event over northern Alabama using Doppler radar data, found strong, organized thunderstorm cells on top of the outflow boundary *behind* the gust front. They noted that these cells were caused by a combination of KHI and internal gravity waves. Specifically, the cells formed along the gust front and propagated backward along the updraft portion of the KHBs. Mueller and Carbone (1987) also observed KHI along an outflow boundary in Colorado. Their Doppler radar data showed circulating billows that formed near the head of the outflow and then propagated backward relative to the front. They found that KHI influenced the formation of arcus clouds over the front, but did not play a direct role in deep convection.

KHI on top of density currents has been simulated using high-resolution mesoscale models. For example, a 2D, dry, slab-symmetric model at 100-m resolution was used by Droegemeier and Wilhelmson (1987) to simulate thunderstorm outflows. Their model captured the explicit turbulent structure of the outflows. Specifically, the turbulence was seen as billows or vortex rolls resulting from KHI. The growth rates, wavelengths, and conditions for onset of the KHBs were found to agree with those of laboratory density currents. However, the use of 2D and idealized initial conditions was a limitation.

TABLE 1. Model parameter settings for domains D1, D2, and D3.

Parameter	D1	D2	D3
Physical domain (km)	96 × 96	32.4 × 19.6	12.9 × 6.5
Horizontal resolution (km)	1.6	0.40	0.10
Vertical resolution*			
dzmin	35 m		
layer of dzmin	Surface–750 m		
model top	10.1 km		
Large time step (s)	4	1.3	0.44
Small time step (s)	2	0.67	0.22
Boundary conditions			
top and bottom*	Rigid		
lateral	Open (wave radiating)		
Coriolis force*	Yes		
Surface physics*	Yes		
Microphysics*	Yes		
Turbulence closure*	Yes (1.5-order turbulent kinetic energy closure)		
Radiation*	Yes (full atmospheric radiative transfer)		
Computational mixing*			
fourth-order vertical	0.0006 s^{-1}		
fourth-order horizontal	0.0001 s^{-1}		
Divergence damping coefficient*			
vertical	0.05		
horizontal	0.05		
Rayleigh damping*			
coefficient	0.053		
Bottom height of sponge layer*	6000 m		

* Values are the same for all grids.

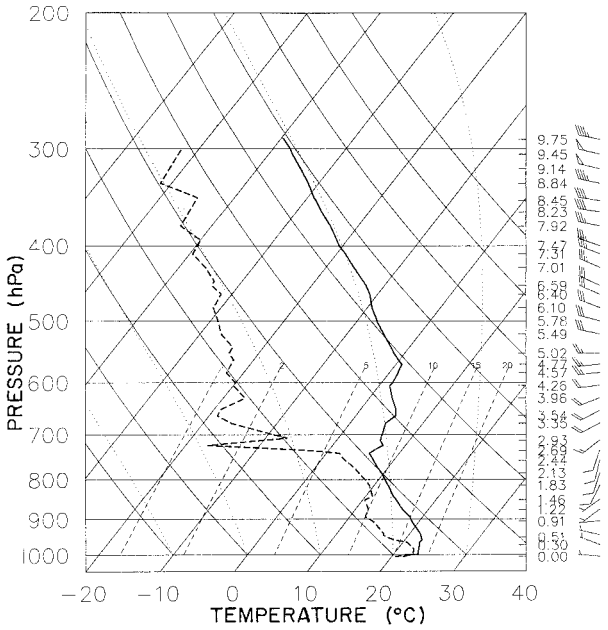

FIG. 3. Cape Canaveral sounding at 1000 UTC 4 Jun 1997 used in conjunction with the Meso-Eta analysis for model initialization. Wind barbs in m s^{-1} (half barb = 5 m s^{-1}).

Sha et al. (1991) investigated interactions between KHI and the sea breeze. Using a 2D, nonhydrostatic model with 100-m horizontal resolution, they simulated the formation of KHBs propagating on top of and behind the sea-breeze head. The KHBs were seen to influence the speed of sea-breeze propagation. Specifically, the simulated sea breeze moved rapidly in the morning, slowed during the day, and accelerated in the evening. They attributed part of the afternoon deceleration to the mixing produced by the circulating billows. Although their results were similar to those of previous laboratory experiments, their work was only in 2D.

Buckley and Kurzeja (1997) performed a 3D numerical study using three grids with two-way interactive nesting to simulate the nocturnal sea breeze (land breeze) near South Carolina. Their grid resolutions were 10.0, 2.5, and 0.657 km, employing full 3D data for initialization. They simulated KHBs on top of and behind the sea-breeze front, but their structure was not consistent with those produced in laboratory experiments (e.g., Simpson and Britter 1979). Additional simulations at higher resolutions (~200 m) produced KHBs with characteristics closer to those of theory, but they still were not as realistic as simulations with resolutions near 100 m (e.g., Sha et al. 1991). Comparisons with observations indicated that the model captured general features of the nocturnal sea breeze. However, the use

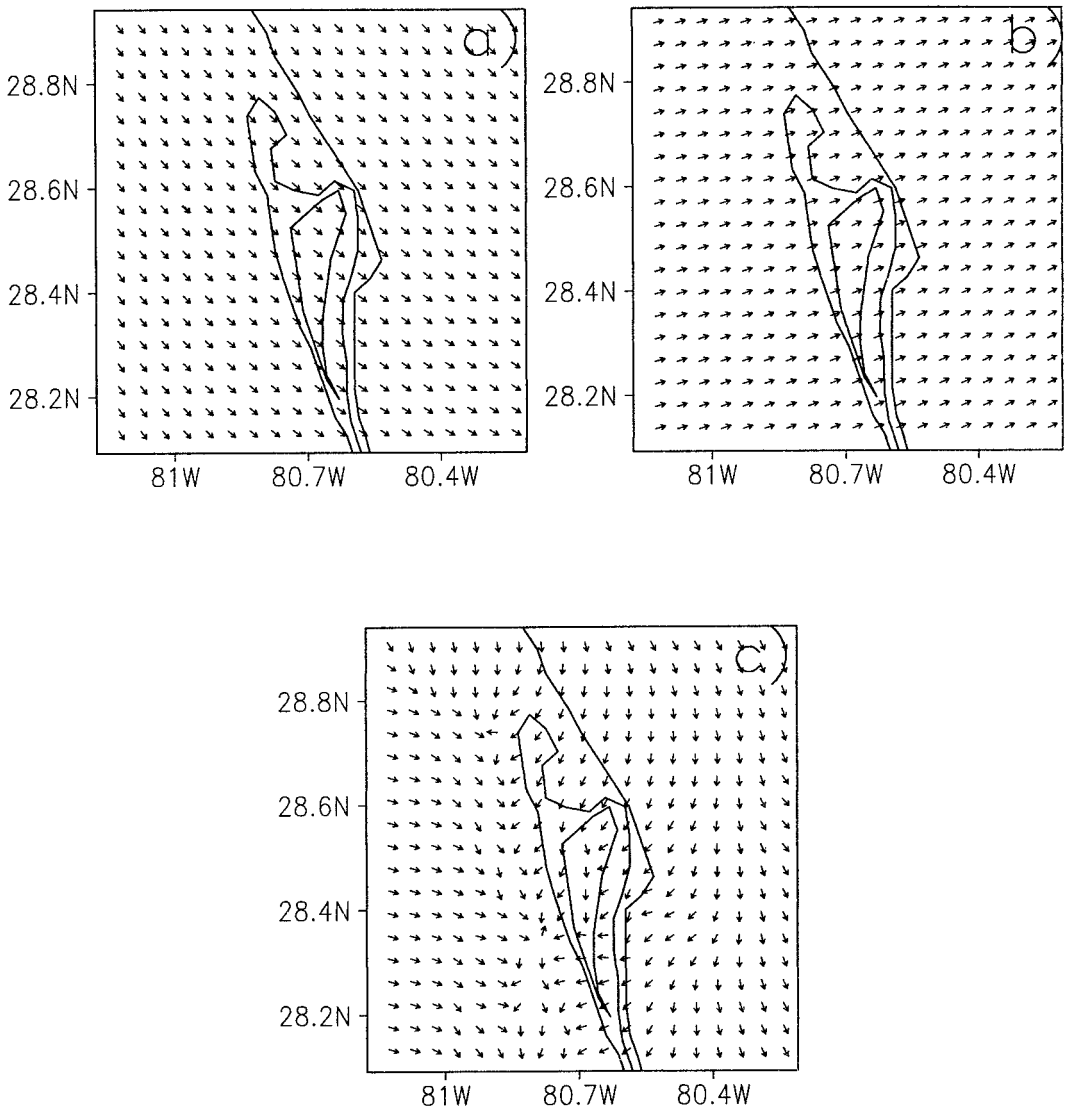

FIG. 4. Winds at (a) 18 m and (b) 4.39 km above the surface within D1 at 0:00. (c) Winds at 18 m above the surface within D1 at 3:56.

of uniform soil type and soil moisture for initialization was a potential limitation of their work.

This paper presents results from high-resolution numerical simulations near Cape Canaveral, Florida. The region exhibits a complex land–sea interface that can produce interesting interactions between land–water circulations (Fig. 1). Land features include mainland Florida, Merritt Island, and Cape Canaveral, while water bodies include the Indian and Banana Rivers, the Atlantic Ocean, and Mosquito Lagoon. The goal is not to forecast a specific event. Rather, we examine the role of KHI in creating preferred areas for convection *behind* the land–water circulations. The findings will further our understanding of sea-breeze convection and may provide useful information to operational meteorologists in coastal areas.

2. Model description and initialization

The Advanced Regional Prediction System (ARPS), developed at the Center for Analysis and Prediction of Storms at the University of Oklahoma, was used in this research. ARPS is a nonhydrostatic, compressible model designed for use at both small scales (e.g., tens of meters) and large scales (e.g., tens of kilometers). One-, two-, and three-dimensional configurations are available. Several options for turbulence closure, vertical grid stretching, cloud microphysics, surface physics, and radiation are available. In addition, ARPS contains an option for two-way interactive nesting, which allows multiple scales of motion to be simulated concurrently. The ARPS two-way grid options contain no limit on the refinement ratio, size of dimensions, or level of nesting,

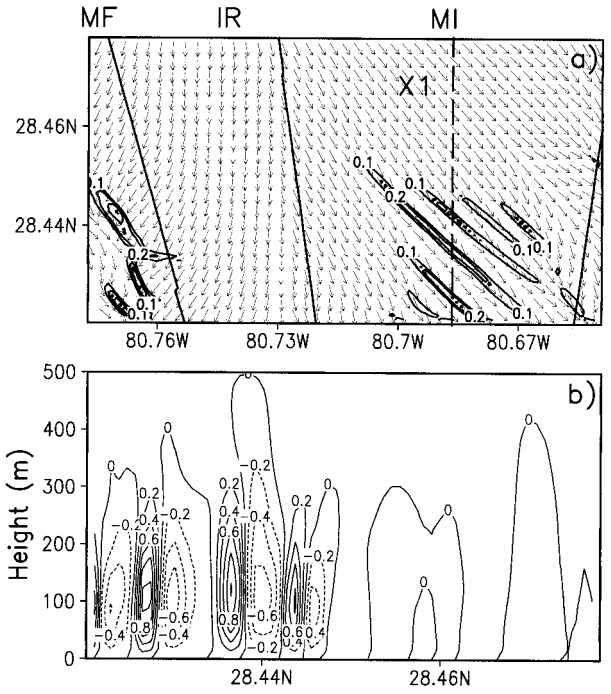

FIG. 5. (a) Upward vertical motion (m s^{-1}) and winds at 18 m above the surface within D3 at 2:36. (b) Cross section (denoted X1 in Fig. 5a) of vertical motion (m s^{-1}). MF denotes mainland Florida, while IR and MI denote locations of the Indian River and Merritt Island, respectively (see Fig. 1).

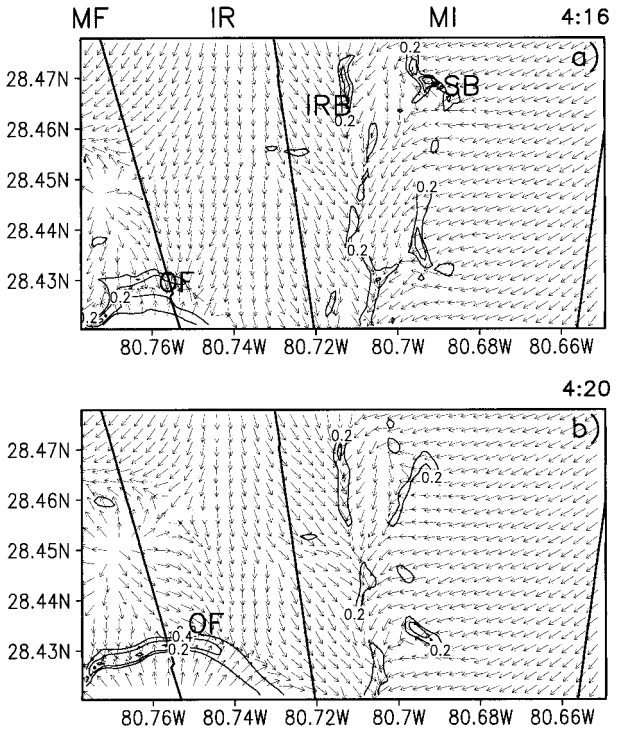

FIG. 6. Upward vertical motion (m s^{-1}) and winds at 18 m above the surface at (a) 4:16 and (b) 4:20. IRB, SB, and OF indicate positions of the Indian River breeze, sea breeze, and outflow boundary, respectively.

and are based on the adaptive grid refinement strategy of Skamarock and Klemp (1993). These features make ARPS an ideal numerical model for high-resolution simulation of boundary layer features. More details of the ARPS and its capabilities can be found in Xue et al. (1995).

The configuration used here is similar to that used in Rao et al. (1999). Specifically, three two-way nested grids were employed (Fig. 2). The outer, middle, and inner grids consisted of, respectively, 60 × 60 grid points at 1.6-km resolution (D1), 81 × 49 grid points at 400-m resolution (D2), and 129 × 65 grid points at 100-m resolution (D3). Grid D1 included all of Merritt Island, Cape Canaveral, and the Indian and Banana Rivers, and extended well into mainland Florida and the Atlantic Ocean. Grid D2 contained parts of Merritt Island, Cape Canaveral, and the mainland. Finally, D3 contained parts of central Merritt Island and mainland Florida and straddled a portion of the Indian River. All three grids contained 35 vertical levels. Within the lowest 750 m, the vertical grid spacing was 35 m, while above 750 m the grid was stretched with an average spacing of 300 m, placing the model top at ~10 km.

The ARPS model can be initialized using either a single sounding or a 3D horizontally inhomogeneous initial state. The ARPS Data Analysis System (ADAS; Brewster et al. 1994) can be used to assimilate various data (e.g., radar, mesonetwork, upper air) within a background field (e.g., other model output, previous ARPS run) for model initialization. The background field used here was the 1200 UTC analysis from the National Centers for Environmental Prediction mesoscale Eta Model (Black 1994). This model output then was interpolated down to our outermost ARPS grid and blended with the 1000 UTC Cape Canaveral sounding using ADAS. The finer-resolution grids (i.e., D2 and D3) were initialized by interpolation from their parent grid (i.e., D2 was initialized from D1, and D3 was initialized from D2). The model then was run in a two-way nested mode for 7 h. The use of full 3D data for initialization was chosen to obtain the most realistic solution possible.

Implementation of the surface characteristics (e.g., soil type, vegetation, soil moisture, water temperatures) and boundary conditions are identical to those used in Rao et al. (1999). Table 1 contains important model settings used for the simulation described in this paper.

3. Results

Satellite imagery of the Cape Canaveral region indicates that postfrontal convection occurs ~15% of the days that exhibit a sea breeze. Data from a representative postfrontal day, 4 June 1997, were used to initialize our simulation. The simulation produced a storm behind the sea-breeze front that formed along an outflow boundary that moved into the area of interest. Although the trig-

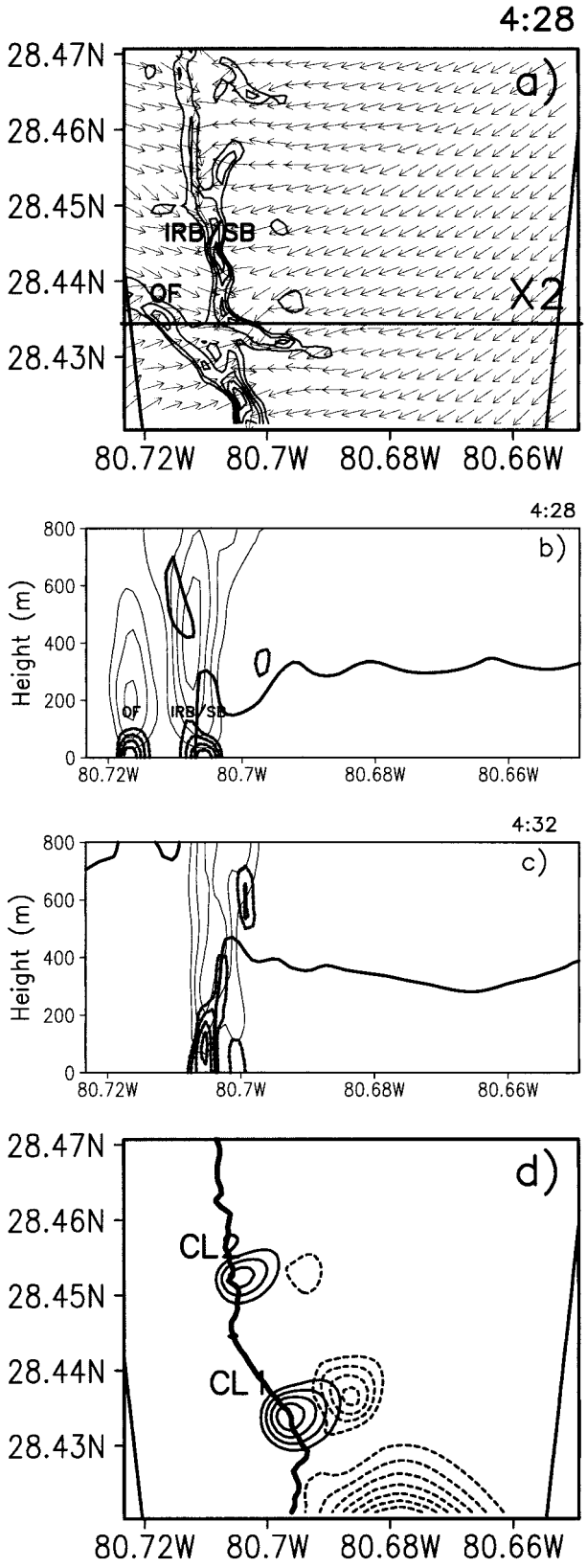

FIG. 7. (a) Upward vertical motion (m s^{-1}) and winds at 18 m above the surface at 4:28 within a portion of D3. Contours range from 0.2 to 1.2 m s^{-1} with an interval of 0.2 m s^{-1}. (b) Cross section of upward vertical motion (m s^{-1}) (thin solid lines) and convergence (s^{-1}) (thick dashed lines) (denoted X2 in Fig. 7a) at 4:28. Vertical motion contours range from 1 to 4 m s^{-1} with an interval of 1 m s^{-1}. Convergence contours range from 0.01 to 0.04 s^{-1} with an interval of 0.01 s^{-1}. (c) As in (b) but at 4:32. Vertical motion (convergence) contours range from 2 to 6 m s^{-1} (0.01–0.04 s^{-1}). (d) Solid (dashed) lines indicate upward vertical motion at 2.1 km above the surface (accumulated rainfall) at 4:40 (4:52). Contours of upward motion (accumulated rainfall) range from 3 to 12 m s^{-1} (0.5–4.0 mm) with an interval of 3 m s^{-1} (0.5 mm). IRB/SB and OF in (a) and (b) indicate positions of the IRB and SB merger and outflow boundary, respectively. Thick, solid lines in (b), (c), and (d) indicate position of zero *u*-wind isotach. CL1 and CL2 in (d) indicate position of cells 1 and 2 discussed in text.

gering mechanism for the cell is obvious (i.e., the outflow boundary), it is not clear why the cell occurred at the precise location and time along the outflow. These questions are investigated in this paper.

Figure 3 presents the thermodynamic profile from Cape Canaveral at 1000 UTC 4 June 1997, which was used in conjunction with the Eta Model analysis for initialization. The winds have a westerly component throughout the depth of the atmosphere, with speeds near 5 m s^{-1} in the lowest levels. The surface temperature is ~21°C, with a thin nocturnal inversion at ~1000 hPa. Another inversion is present near 700 hPa, indicating a stable region in the middle troposphere. Below this inversion, the air is relatively moist, with dewpoint depressions ranging from 2° to 4°C. Conversely, the atmosphere shows significant drying above.

Figure 4 shows the horizontal winds in D1 at 18 m (Panel a) and 4.39 km (Panel b) above the surface at model initialization. The winds at 18 m above the surface, but at 3 h, 56 min into the simulation, also are shown (Fig. 4c). (Hereafter, time into the simulation will be denoted as hh:mm, e.g., 3:56 signifies 3 h, 56 min into the simulation.) At the initial model time, winds generally are from the northwest near the surface (Fig. 4a) but are almost due westerly in the midtroposphere (Fig. 4b). By 3:56 (Fig. 4c), winds in the midtroposphere change little (not shown), but winds near the surface show the complex land–water circulations common to the area. Specifically, over the southern part of the domain, the sea breeze is evident as the area of surface convergence near 80.70°W. Over Merritt Island, the winds have a more northerly component (i.e., less of an easterly component) compared to areas farther north and south. This wind pattern is a result of an eastward moving Indian River breeze (IRB) and has been denoted the ''Merritt Island effect'' (Lyons et al. 1992). Specifically, the eastward-moving IRB collides with the westward moving sea breeze to create an area of enhanced convergence that prevents the sea breeze from reaching mainland Florida. These multiple land–water circulations suggest that complex interactions over Merritt Island are likely during the simulation.

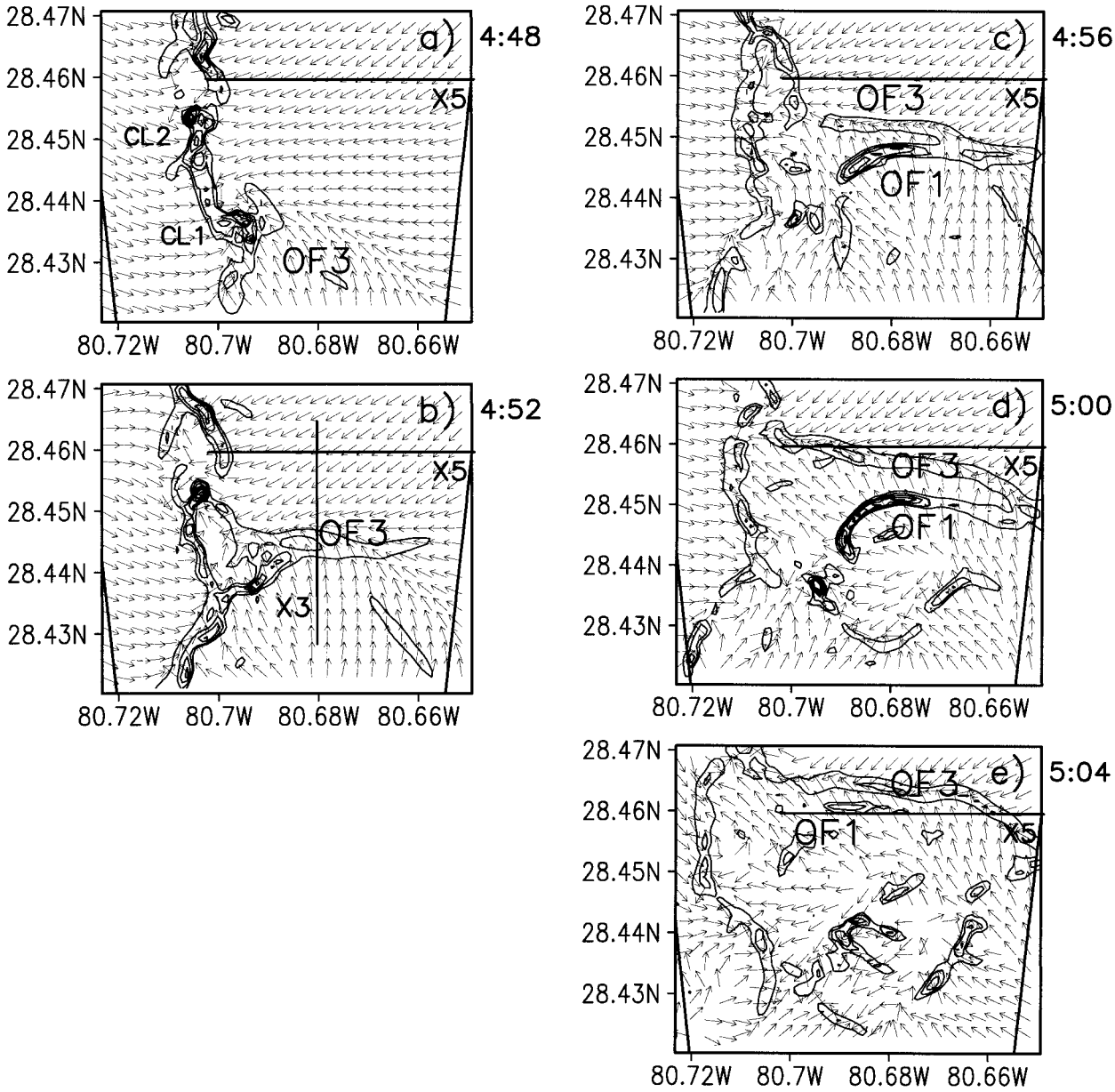

FIG. 8. Upward vertical motion (m s^{-1}) and winds at (a) 4:48, (b) 4:52, (c) 4:56, (d) 5:00, and (e) 5:04 at 88 m above the surface. Minimum contour is 1 m s^{-1}. Contour interval is 1 m s^{-1}. OF1 and OF3 indicate positions of outflow boundaries discussed in text. X5 denotes cross section discussed in Figs. 13 and 15. X3 denotes cross section discussed in Fig. 9.

a. Convection along the sea-breeze front

The location of our innermost grid (D3, Fig. 2) allows interactions over Merritt Island to be studied in detail. Figure 5a shows upward vertical motion and horizontal winds at 18 m above the surface at 2:36. Over the southwestern corner of the domain (over mainland Florida), relatively strong upward motion is associated with the westward-moving IRB. This movement is consistent with the easterly component of the surface winds in this area. The wind pattern indicates only a weak eastward-moving IRB on the eastern shoreline of the Indian River. Specifically, the winds exhibit a slight change in direction near the eastern shore of the Indian River.

Elongated regions of upward motion are oriented northwest to southeast over Merritt Island. These circulations are aligned along the mean boundary layer wind and are spaced ~600 m apart. A north–south cross section of vertical motion intersecting the circulations (Fig. 5b, denoted X1 in Fig. 5a) shows that ascent reaches ~1 m s^{-1}. The counterrotating circulations extend to the top of the boundary layer (~300 m based on the virtual temperature), producing an aspect ratio of ~2.0.

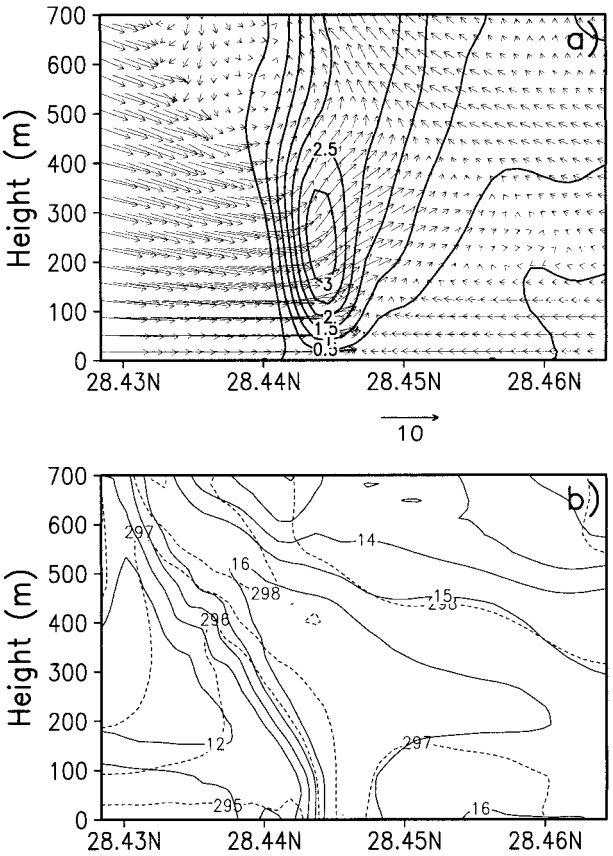

FIG. 9. (a) Upward vertical motion (m s^{-1}) and v–w windflow, and (b) potential temperature (K, dotted lines) and mixing ratio (g kg^{-1}, solid lines) along X3 at 4:52. Axis of X3 is shown in Fig. 8b.

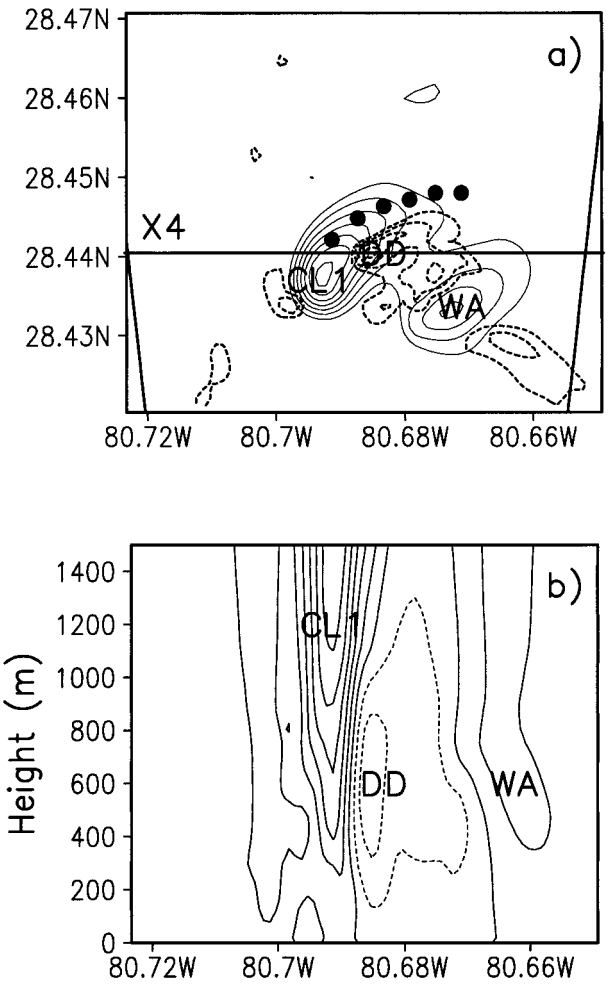

FIG. 10. (a) Upward vertical motion (solid) at 2.1 km above the surface at 4:56. Also shown is the downward vertical motion (dashed) at 500 m above the surface. Contours range from −8 to 14 m s^{-1}, with an interval of 2 m s^{-1}. CL1 indicates updraft of cell 1, while DD indicates the downdraft produced by CL1. Here, WA indicates position of weak ascent discussed in text. The thick dotted line indicates the surface position of OF1 at 4:56. (b) Cross section of vertical motion (m s^{-1}) denoted X4 in top panel. Values range from −6 to 15 m s^{-1}, with an interval of 3 m s^{-1}. CL1, DD, and WA indicate the same features as in the top panel.

This value, along with the horizontal structure and orientation of the features, are consistent with those of HCRs (Atkins et al. 1995; Weckwerth et al. 1996). The HCRs grow in size as daytime heating increases (i.e., as the boundary layer deepens) but, eventually, are destroyed by a westward-moving sea breeze (discussed next).

Figure 6 shows upward vertical motion and horizontal winds within D3 at 18 m above the surface at 4:16 (panel a) and 4:20 (panel b). As discussed above, the HCRs no longer are evident. However, both the wind and vertical motion patterns indicate several other boundary layer convergence zones. Over central Merritt Island at 4:16 (Fig. 6a), the westward-moving sea-breeze front is indicated by a discontinuous north–south line of upward motion (labeled SB). The eastward-moving IRB, barely noticeable at 2:36 (Fig. 5a), has strengthened and now is indicated by the region of upward motion just west of the SB (labeled IRB). These two land–water circulations are merged over the southern part of the domain. Near the west-central edge of the domain, the wind field indicates a downdraft produced by a thunderstorm along the western segment of the IRB (over the mainland, west of the domain). However, the leading edge of this outflow boundary exhibits relatively small upward motions (i.e., less than 0.2 m s^{-1} at 18 m). An outflow boundary with much stronger ascent is located over the southwestern corner of the domain (labeled OF, Fig. 6a). The OF is the result of a thunderstorm that formed along the westward-moving IRB, but south of D3.

At 4:20 (Fig. 6b), the IRB and SB are harder to differentiate since the two boundaries are now closer together. Their closer proximity is due mainly to the SB. Specifically, the IRB remains nearly stationary during the previous 4 min, while the SB generally moves westward at ~4 m s^{-1}. The OF, which was just entering D3 at 4:16, now is clearly evident over the southwestern portion of the domain, traveling at a speed of ~7 m

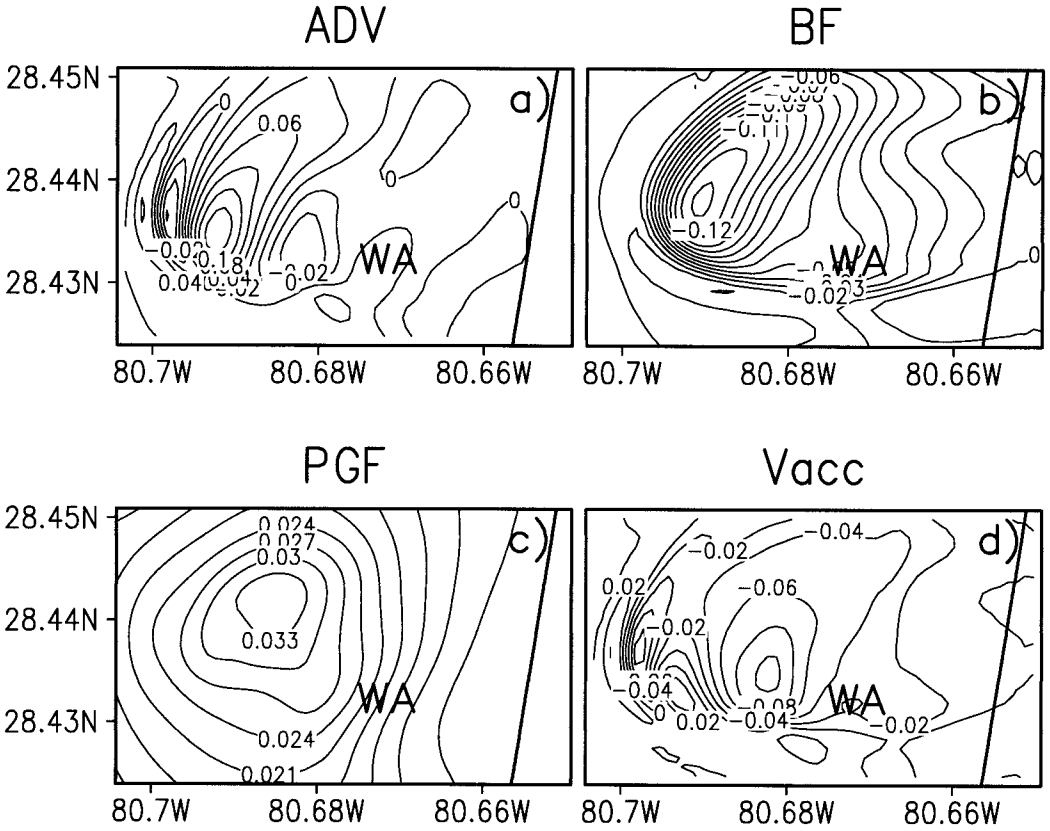

FIG. 11. (a) Three-dimensional advection of vertical momentum, (b) buoyancy force, (c) perturbation pressure gradient force, and (d) net vertical acceleration 4.3 km above the surface at 4:56. All values are in m s^{-2}. Here, WA indicates feature discussed in Fig. 10.

s^{-1}. The greatest ascent in OF is located along its merger with the outflow boundary to its north (values exceed 0.4 m s^{-1} near 28.43°N, 80.76°W). The locations and movements of the IRB, SB, and OF suggest that a collision over Merritt Island is imminent. Density currents frequently collide over Merritt Island because the heat source (i.e., Merritt Island) is surrounded by cooler water bodies (Lyons et al. 1992).

Figure 7a focuses on the region of Merritt Island where the three boundaries are colliding. Specifically, it shows upward vertical motion and winds at 18 m above the surface over a portion of D3 at 4:28. The IRB and SB are merged within most of the domain (Fig. 7a, denoted IRB/SB). In addition, the OF is merged with the land–water circulations over the southern portion of the domain. Vertical motions within this merger are ~0.2 m s^{-1} larger than those farther north where the OF has yet to arrive. To investigate the consequence of the OF merger, cross sections of upward vertical motion and convergence (axis denoted X2 in Fig. 7a) were prepared just before (4:28) and after (4:32) the OF consolidation. Prior to merger (i.e., 4:28, Fig. 7b), there are two maxima of upward motion and low-level convergence. Upward motion reaches 3 m s^{-1} along the OF, while exceeding 4 m s^{-1} within the land–water circulations. After the merger (Fig. 7c), only one updraft is present, with values in excess of 6 m s^{-1}. In addition, the collision increases the depth of the SB head from ~300 m at 4:28 (Fig. 7b) to ~500 m at 4:32 (Fig. 7c).

The collision of outflow boundaries with other convergence zones has been shown to trigger new convective storms (e.g., Purdom 1982; Wilson and Schreiber 1986). In the current simulation, a precipitating storm (CL1) develops along the merged boundaries near 28.435°N, 80.7°W (i.e., along X2, Fig. 7a). In addition, a second cell (CL2) forms farther north after the OF merges with the land–water circulations in that region. These two cells are evident in the upward vertical motion at 2.1 km above the surface at 4:40 (solid lines, Fig. 7d). CL1 (2) has values near 12 m s^{-1} (9 m s^{-1}) at ~2.1 km. By 4:52, liquid water within each cell has begun to reach the surface (dashed lines, Fig. 7d). The difference in updraft intensity and accumulated rainfall between the two cells is due to the time of OF merger. Specifically, CL1 forms before CL2 since the trigger (i.e., the OF merger) occurs at an earlier time. Thus, CL1 is at a later stage of development than CL2.

A third area of rain is located near the southernmost edge of the domain (Fig. 7d). This rain was produced by a storm that formed south of D3 (CL3, not shown)

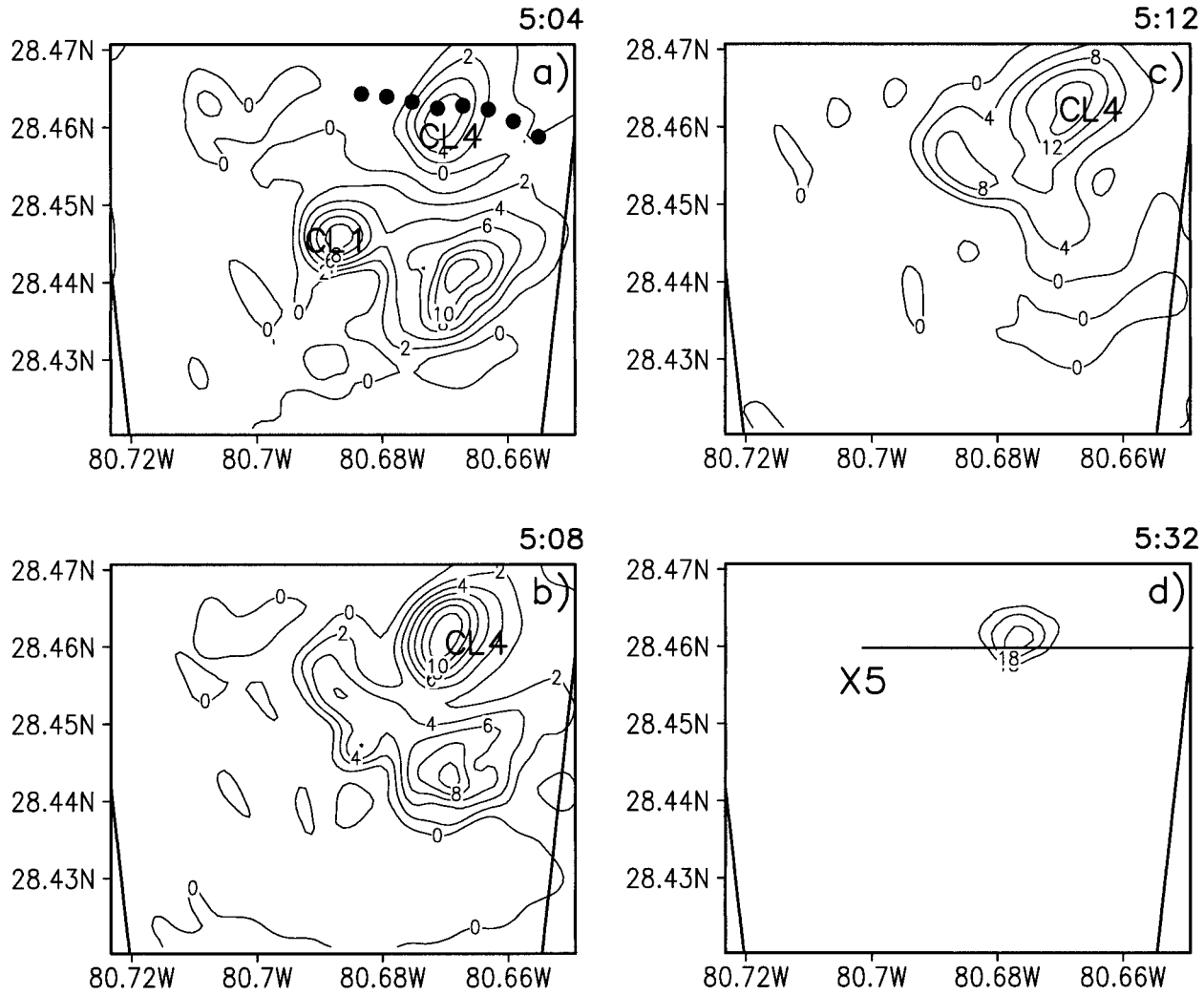

FIG. 12. Upward vertical motion (m s^{-1}) 2.1 km above the surface at (a) 5:04, (b) 5:08, and (c) 5:12. (d) Accumulated rainfall (mm) greater than 15 mm at 5:32. CL1 and CL4 indicate the positions of cell 1 and cell 4, respectively. The thick dotted line in (a) denotes the surface position of OF3 at 5:04. X5 in (d) indicates the location of the cross section discussed in Figs. 13 and 15.

along the sea-breeze front. An outflow boundary produced by CL3 is important in convective development behind the sea-breeze front within D3. That scenario is described next.

b. Postfrontal convection

Figure 8 shows upward vertical motion and horizontal winds at 88 m above the surface at 4:48 (panel a), 4:52 (panel b), 4:56 (panel c), 5:00 (panel d), and 5:04 (panel e). At 4:48 (Fig. 8a) convergence associated with the SB front is evident along ~80.7°W. The complex vertical motion pattern near 28.435°N is due to the storm described earlier (i.e., CL1 in Fig. 7d). Farther north along the SB front, near 28.455°N, CL2 is indicated by the relative maximum in vertical motion. Along the southern portion of the domain, the winds indicate an outflow boundary moving into D3 (labeled OF3). OF3 is produced by CL3 that was discussed in the previous section (Fig. 7d). At 4:52 (Fig. 8b), vertical motion associated with OF3 increases as the boundary moves northward. These vertical motions exceed 2 m s^{-1} at lower levels in some regions. The vertical structure of OF3 within the boundary layer is presented in a north–south cross section intersecting the outflow at 4:52 (Fig. 9, denoted X3 in Fig 8b). Vertical motions are greatest just above the region of maximum surface convergence (Fig. 9a, near 28.445°N), with values exceeding 3 m s^{-1} at 300 m above the surface. Air within the outflow boundary exhibits potential temperature (mixing ratio) values that are ~2 K (~3 g kg^{-1}) less than those of the surrounding environment (Fig. 9b). These characteristics are expected within the cool and dry downdraft air.

The flow pattern within D3 has grown more complex by 4:56 (Fig. 8c). Specifically, another outflow (labeled OF1) now is present. OF3 and OF1 are separate regions

of upward motion just east of the SB front, but they are combined along the eastern portion of the domain. To determine the origin of OF1 we prepared a horizontal analysis of upward (downward) motion at ~2.1 km (500 m) above the surface at 4:56 (Fig. 10a). The strong updraft of CL1 is seen clearly near 28.44°N, 80.69°W (solid lines, labeled CL1). Just east of the CL1 updraft, its associated downdraft is evident at 500 m (labeled DD). Descent exceeding 8 m s^{-1} is present in this region. The updraft–downdraft couplet also is evident in a cross section of vertical motion intersecting the storm (Fig. 10b, denoted X4 in Fig. 10a). The subsiding air (DD) is located adjacent to and slightly below the core of CL1. A portion of OF1 is indicated in Fig. 10a as the dotted line. Comparison of the orientation and position of OF1 and DD suggests that outflow boundary OF1 is a product of the downdraft from storm CL1. In addition, the close proximity between OF1 and DD (i.e., ~300 m) indicates that OF1 is in the early stages of its lifetime. This explains why OF1 was not evident 4 min earlier (Fig. 8b).

An area of somewhat weaker ascent is located southeast of CL1 near 28.43°N, 80.67°W (labeled WA in Fig. 10). This updraft was initiated by OF3 approximately 8 min earlier, but the area never develops into a precipitating storm. To determine why no further development occurred, we considered the model formulation of vertical acceleration,

$$\frac{\partial w}{\partial t} = -\underbrace{\left(u\frac{\partial w}{\partial x} + v\frac{\partial w}{\partial y} + w\frac{\partial w}{\partial z}\right)}_{\text{ADV}} - \underbrace{\frac{1}{\rho}\frac{\partial p'}{\partial z}}_{\text{PGF}} + g\left[\underbrace{\frac{\theta'}{\theta}}_{\text{BF1}} + \underbrace{\frac{q_v'}{\varepsilon + q_v}}_{\text{BF2}} - \underbrace{\frac{q_v' + q_{\text{liquid+ice}}}{1 + q_v}}_{\text{BF3}}\right] + \underbrace{\text{turb}}_{\text{TD}} + \underbrace{\text{cpm}}_{\text{CM}}, \quad (1)$$

where q_v is the water vapor mixing ratio, θ the potential temperature, ε the ratio of the gas constants for dry air and water vapor, $q_{\text{liquid+ice}}$ the total liquid and ice water content, and g the acceleration due to gravity, while primes denote perturbation values. [Others also have utilized model components of vertical acceleration in their analyses (e.g., Carpenter et al. 1998; Trier et al. 1997).] The terms on the right-hand side of (1) represent the three-dimensional advection of vertical momentum (ADV), vertical perturbation pressure gradient force (PGF), buoyancy force (BF1–BF3), turbulence diffusion (TD), and computational mixing (CM), respectively. The buoyancy force can be partitioned into components representing thermal buoyancy acceleration (BF1) plus vapor buoyancy acceleration (BF2) minus condensate loading (BF3). The net acceleration is just the sum of these terms.

Figure 11 shows the individual terms and the net acceleration at 4:56 approximately 4.3 km above surface in the region surrounding CL1 (TD and CM are not shown since they are an order of magnitude smaller than the remaining terms). The three-dimensional advection term (Fig. 11a) exhibits large gradients near CL1; that is, vertical momentum is advected both vertically and horizontally near the core of the updraft. There are small positive values near the area of weak ascent (WA in Fig. 11). The total buoyancy force (Fig. 11b) is negative over much of the domain. This is due mainly to subsidence from CL1 that results in midlevel warming (resulting in a large negative thermal buoyancy term). The downward acceleration due to the buoyancy force will coincide with high (low) perturbation pressures below (above) and result in an upward-directed (positive) perturbation pressure gradient force (Fig. 11c). However, these positive values are not large enough to overcome the negative buoyancy near WA (Fig. 11d), and the combination of the forces results in negative vertical accelerations in that area. Thus, negative buoyancy associated with subsidence from CL1 appears to suppress development within WA.

We now return to describing the evolution of outflow boundaries (Fig. 8). At 5:00 (Fig. 8d), both OF3 and OF1 are moving northward. The wind pattern shows that the downdraft of CL1 now is located near 28.44°N, 80.675°W. OF3 remains well defined at 5:04 (Fig. 8e), extending from the SB front on the west to the eastern edge of the domain. However, OF1 is evident only as small regions of upward motion behind OF3 (e.g., near 28.46°N, 80.69°W and near 28.45°N, 80.7°W). The dissipation of OF1 may be due to the weak opposing flow just behind OF3. Specifically, this portion of OF1 is moving northward in a region of southerly flow (i.e., behind OF3). Hence, the surface convergence is relatively modest and upward motion weak.

OF3 triggers a single precipitating cell behind the sea breeze (near 80.67°W), which begins to develop near 5:04. Why this storm develops at this precise location and time is the focus of the remainder of this paper. Figure 12 shows upward vertical motion at 2.1 km above the surface at 5:04 (panel a), 5:08 (panel b), and 5:12 (panel c). At 5:04, three maxima of upward motion are present. The updraft of CL1 is located near 28.445°N, 80.69°W. Its magnitude has decreased substantially from 8 min earlier (Fig. 10). To its southeast, the updraft initiated previously by OF3 (i.e., WA) still is present (recall that this cell did not precipitate). Its maximum ascent reaches ~13 m s^{-1} near 5:04 and then quickly dissipates. Farther north along OF3, a new updraft (labeled CL4 in Fig. 12a) exhibits vertical motions of ~6 m s^{-1} at 2.1 km. OF3 is located beneath this region of upward motion at 5:04 (dotted line, Fig. 12a), suggesting that OF3 triggered the convection. Four minutes later (i.e., 5:08, Fig. 12b) vertical motion has increased to ~12 m s^{-1} within CL4, while the other updrafts have decreased. By 5:12 (Fig. 12c), CL4 intensifies even further (i.e., ~16 m s^{-1}). Accumulated rainfall at 5:32 (Fig.

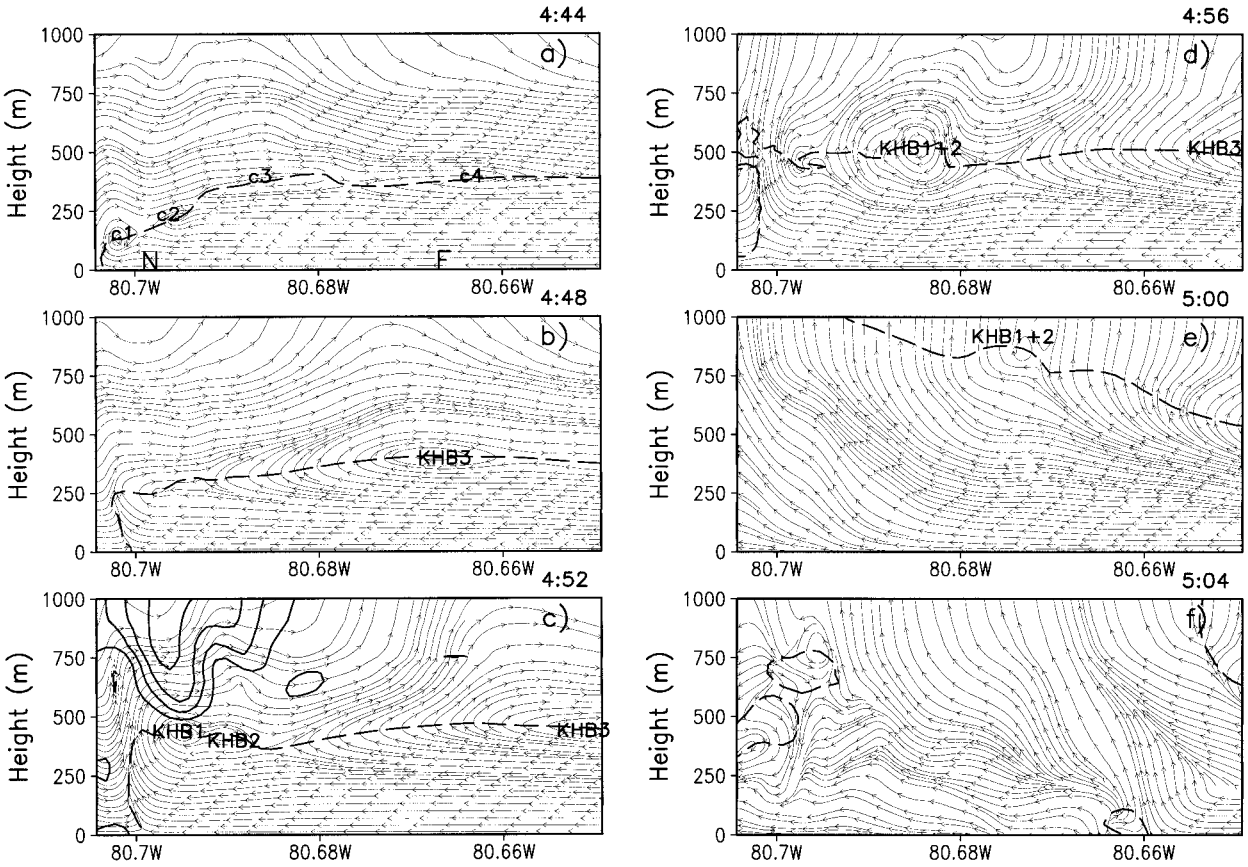

FIG. 13. The *u*–*w* streamlines along X5 at (a) 4:44, (b) 4:48, (c) 4:52, (d) 4:56, (e) 5:00, and (f) 5:04. C1–C4, KHB1–KHB3, and KHB 1+2 indicate locations of circulations discussed in text. The *u*-wind speed (m s^{-1}) at 4:52 is shown as solid lines in (c). Contours range from 2 to 8 m s^{-1}, with an interval of 2 m s^{-1}. Dashed line indicates zero *u*-wind isotach. The axis of X5 is shown in Fig. 12d. Points N and F in (a) indicate locations of Ri profiles discussed in Fig. 14.

12d, only values greater than 15 mm are shown) indicates that CL4 produces substantially more rainfall than any other storm in the region; that is, all others produce less than 15 mm.

The temporal and spatial proximity of OF3 to the initiation of CL4 suggests that OF3 supplies the lifting necessary for convective development. However, similar magnitudes of low-level vertical motion (at 88 m) are located all along OF3 at 5:04 (Fig. 8e). In fact, ascent is somewhat larger west of CL4. In addition, the vertical motion within OF3 changes little between 4:52 and 5:04. Thus, the lift provided by OF3 does not explain why CL4 develops at this particular location and time, and why no development occurs at other nearby locations. We hypothesize that atmospheric structure above the sea-breeze air is critical in determining the time and location of storm development. This hypothesis is investigated in the next section.

c. Initiation of CL4

We investigate atmospheric structure near CL4 using east–west cross sections of vertical motion and *u*–*w* streamlines through its region of maximum rainfall (denoted X5 in Fig. 12d). Figure 13 shows *u*–*w* streamlines along X5 at 4:44 (panel a), 4:48 (panel b), 4:52 (panel c), 4:56 (panel d), 5:00 (panel e), and 5:04 (panel f). Also shown is the zero *u*-wind isotach (this isotach is used to represent the interface between the marine and continental air).

At 4:44 (Fig. 13a) four vortices (labeled C1–C4) are present behind and along the top of the SB front. Their location at the top of the SB interface suggests that they result from KHI. Specifically, previous investigations (e.g., Simpson and Britter 1979; Sha et al. 1991) have shown that KHI can occur in the strong shear zone above density currents. We calculated several parameters to confirm the presence of KHI. The gradient Ri is defined as the ratio of static stability and vertical wind shear; that is,

$$\mathrm{Ri} = \left(\frac{g}{\theta}\right)\left(\frac{\partial\theta}{\partial z}\right)\left(\frac{\partial V}{\partial z}\right)^{-2}. \qquad (2)$$

The value of Ri must be less than 0.25 for KHI to initiate (Miles and Howard 1964), but KHI can persist if Ri is

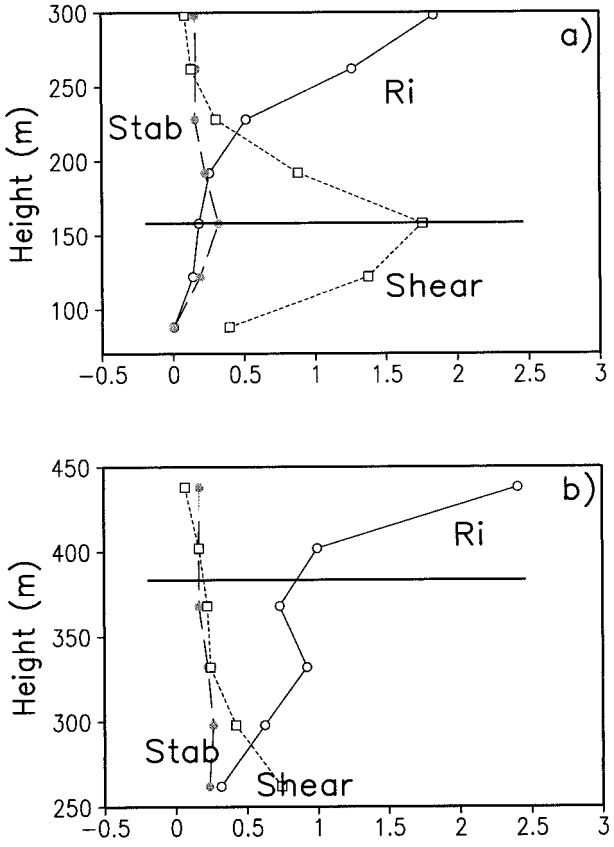

FIG. 14. The gradient Ri, vertical wind shear term (shear, $\times 10^{-3}$ s^{-2}), and stability term (stab, $\times 10^{-3}$ s^{-2}) at points (a) N and (b) F at 4:44. Points N and F are shown in Fig. 13a. The solid horizontal line represents the SB interface.

less than 1.0 (Wallace and Hobbs 1977). Figure 14 presents vertical profiles of Ri, the stability term, and the vertical wind shear term at points near the frontal boundary at 4:44 (panel a, denoted N in Fig. 13a) and another location farther back along the SB interface (panel b, denoted F in Fig. 13a). The stability term exhibits little change across the SB interface (denoted by the horizontal line) at both locations (Fig. 14). However, the vertical wind shear term at the SB interface is nearly twice as large near the frontal location (point N, Fig. 14a) than farther back near point F (Fig. 14b). This results in lower Ri values closer to the front (i.e., ~0.18 at point N vs ~0.90 at point F). These values meet the necessary criterion for KHI to initiate near the frontal location and persist as it propagates backward relative to the front.

Wavelengths of KHBs have exhibited a wide range of values, typically varying from 0.5 (Sha et al. 1991) to 20 km (Buckley and Kurzeja 1997). Inspection of the vortices (Fig. 13a) indicates that current wavelengths are within this range, that is, ~500 m between C1 and C2, increasing to ~2 km between C3 and C4.

The wavelengths of KHBs strongly depend on the thickness of the shear layer in which the KHBs evolve. Specifically, the horizontal wavelength of the fastest-growing perturbation in a shear layer of thickness h has been shown to range from 4.4 h (Drazin 1958) to 7.5 h (Miles and Howard 1964), and has been used to quantify the existence of KHI (Droegemeier and Wilhelmson 1987; Mueller and Carbone 1987; Sha et al. 1991). Although difficult to objectively determine due to the continual evolution of the 3D wind field, h at the current time (i.e., 4:44) ranges from ~200 to 300 m based on the gradient of the vertical shear (not shown). This results in wavelengths ranging from ~880 m to ~2.5 km, similar to those shown in Fig. 13a.

Finally, KHI can be quantified by calculating the ratio between the maximum amplitude and horizontal wavelength of the billows. This ratio is very sensitive to static stability, with larger values in neutral or near-neutral environments (Mueller and Carbone 1987). Previous work has shown this ratio to range from 0.01 (e.g., Buckley and Kurzeja 1997) to 1.0 (e.g., Britter and Simpson 1978). Our mean value of 0.16 falls within this range. Based on the above parameters, we believe that circulations C1–C4 along the top of the sea-breeze interface most likely result from KHI.

Between 4:44 and 5:00 (Figs. 13a–e), the circulations continually evolve as they propagate backward relative to the front. This is especially evident in computer animations. For example, KHB 3 (i.e., C3) grows in amplitude and moves eastward along the top of the SB. By 4:56 (Fig. 13d), only the western most portion of its circulation is present along X5. KHBs 1 and 2 are difficult to identify at 4:48 (Fig. 13b); however, the individual circulations become more distinct 4 min later (Fig. 13c). Then, between 4:52 and 4:56, KHBs 1 and 2 combine to produce a larger and better-defined billow (denoted KHB 1+2 in Fig. 13d). The merger of these billows is a result of greater westerly winds above KHB 1 than above KHB 2 (solid lines, Fig. 13c). Specifically, the u-wind velocity indicates an axis of large westerly winds located directly above KHB 1. Since KHBs typically move with the mean wind near their altitude of maximum amplitude (Houze 1993), KHB 1 moves eastward at a faster rate than KHB 2. Thus, KHB 1 eventually reaches KHB 2, resulting in the merger of the two circulations. This finding is consistent with previous work that investigated the aggregation of small-scale vortices (e.g., McWilliams 1990; Christiansen and Zabusky 1973).

The consolidation of the KHB 1 and 2 creates a single, better-defined, and larger circulation (KHB 1+2, Fig. 13d). This region of enhanced westerlies above the sea air (Fig. 13c) is a result of flow around CL2, and will be discussed later. At 5:00 (Fig. 13e), KHB 1+2 still is evident along the SB interface near 80.675°W. However, by 5:04 (Fig. 13f), its circulation no longer is present. The complex structure and mutual interaction of the KHBs just discussed is not unexpected in a 3D high-resolution simulation. Specifically, small-scale

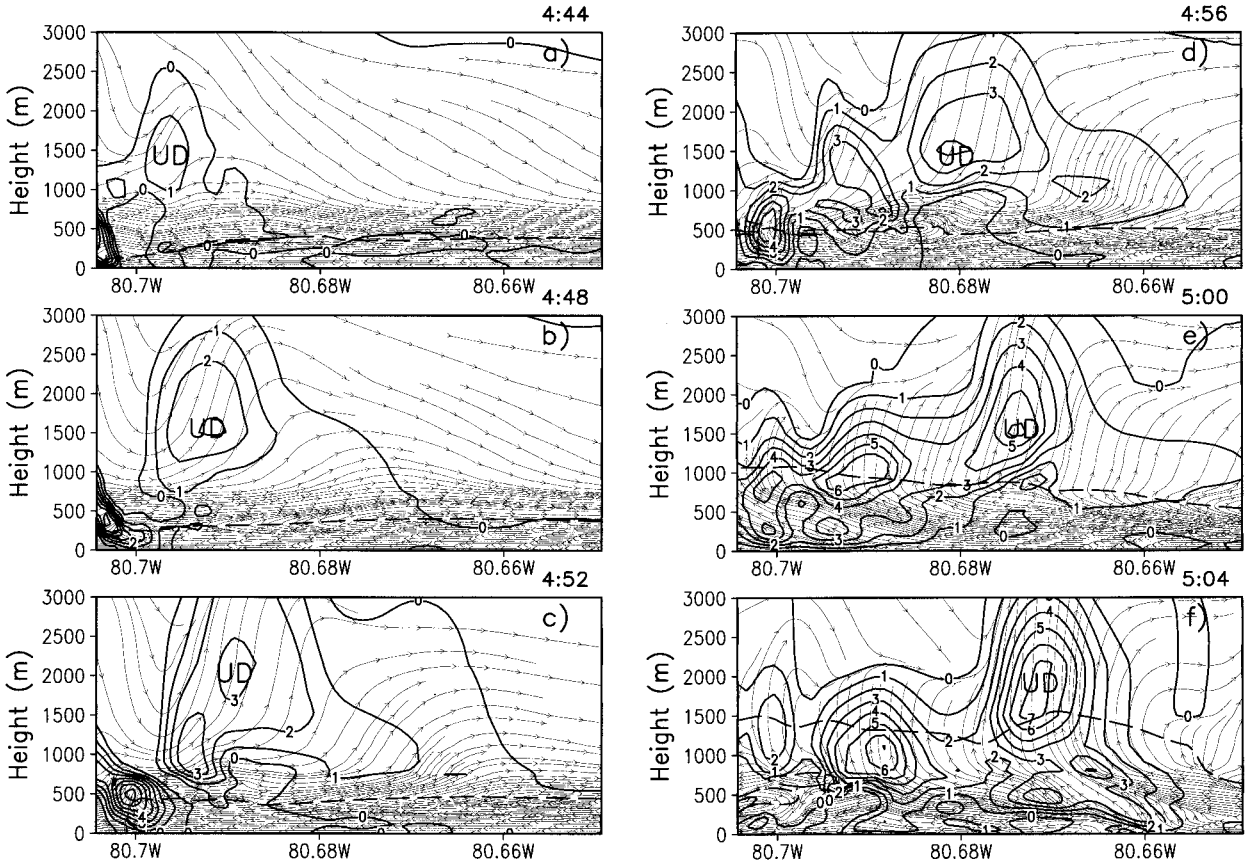

FIG. 15. As in Fig. 13 but including upward vertical motion (solid lines, m s^{-1}). Also note the different vertical scale. Here UD indicates position of updraft discussed in text.

changes in the wind flow can alter both the propagation speed and structure of individual KHBs.

The streamline pattern in Fig. 13 suggests a complex vertical motion field. To investigate the effect of this on the development of CL4, vertical motion was plotted along X5 (Fig. 15). Figure 15 is similar to Fig. 13, but with a greater height scale and the addition of upward vertical motion. Relatively large values of ascent are located near the SB front (i.e., left edge of the domain) between 4:44 and 4:56 (Figs. 15a–d). Specifically, maximum values of upward motion reach ~6 m s^{-1} near the frontal location during these times. Farther east and below the SB front (i.e., within the marine air), upward motion generally is less than 1 m s^{-1} between 4:44 and 4:56 (Figs. 15a–d). This is expected in the comparatively stable sea air. However, by 5:00 (Figs. 15e), the vertical motion near the surface along X5 increases considerably from just 4 min earlier. Specifically, within the western portion of the marine air (e.g., near 80.69°W), there now is relatively large upward motion near the surface (~200 m) behind the SB front. Values as great as 4 m s^{-1} are present in this region. This increase in upward motion is due to OF3, which is moving northward. OF3 is oriented slightly northwest–southeast (Fig. 8d), thereby explaining why low-level ascent only increases along the western portion of X5 at 5:00 (i.e., OF3 has yet to reach the eastern portion of X5). By 5:04 (Fig. 15f), OF3 continues its northward movement (Fig. 8e) affecting the eastern portion of X5 as it did the western portion 4 min earlier (Fig. 15e). An axis of strong upward motion tilts westward from the surface (near 80.66°W) to higher altitudes (UD). This region soon develops into the strong updraft of CL4 (Fig. 12). The disappearance of KHB 1+2 at 5:04 (Fig. 13f) is attributed to this region of ascent.

As just mentioned, UD developed into the updraft of CL4. Therefore, we next explore the evolution of UD in detail. This relatively deep layer of ascent (maximum values generally above ~900 m) is located above the marine air (labeled UD in Figs. 15a–f). Between 4:44 (Fig. 15a) and 4:48 (Fig. 15b), the region of ascent moves slightly eastward; for example, the maximum near 1.5 km is located at ~80.7°W (~80.69°W) at 4:44 (4:48). Between 4:48 (Fig. 15b) and 4:52 (Fig. 15c), UD expands along X5 (note the 2 m s^{-1} contour between 4:48 and 4:52). In addition, a new relative maximum of upward motion is present at ~900 m near 80.695°W.

To determine the origin and structure of UD, horizontal analyses of upward motion and wind vectors were prepared over a portion of D3 at 1.5 km (Fig. 16). (Note

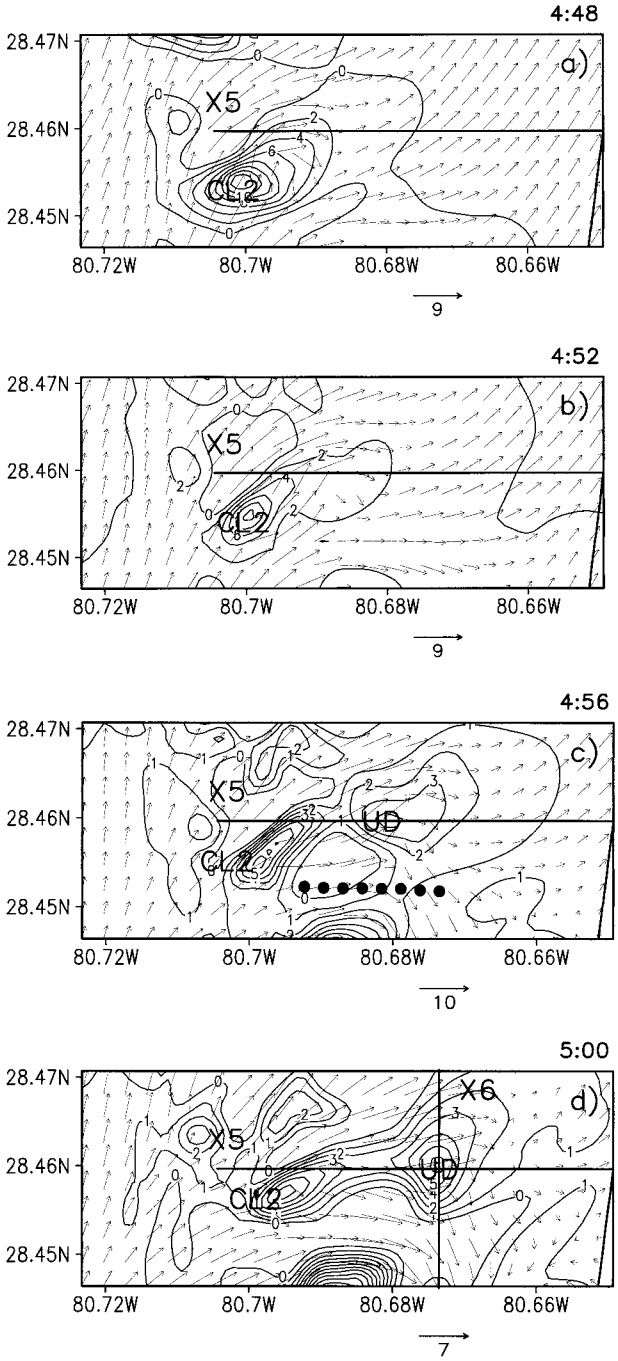

FIG. 16. Upward vertical motion (m s^{-1}) and winds at 1.5 km above the surface at (a) 4:48, (b) 4:52, (c) 4:56, and (d) 5:00. Contour interval in (a) and (b) is 2 m s^{-1}, while interval in (c) and (d) is 1 m s^{-1}. X5 indicates cross section discussed previously. CL2 denotes location of cell 2. Here UD corresponds to the updraft discussed in Fig. 15. X6 denotes cross section discussed in Fig. 21. Thick dotted line in (c) indicates surface position of OF3.

that a smaller portion of D3 is shown compared to Fig. 12.) At 4:48 (Fig. 16a), CL2 is located near 28.455°N, 80.7°W with maximum updrafts exceeding 14 m s^{-1}. [Recall that CL2 was triggered by a collision between the SB and OF (Fig. 7).] The updraft of CL2 exhibits a slight southwest–northeast orientation at 4:48 (Fig. 16a). The location of UD along X5 at 4:48 (i.e., near 1.5 km, 80.69°W, Fig. 15b) is attributed to this orientation. Wind vectors indicate that the environmental flow moves around the updraft of CL2, accelerating as it moves past the region of ascent. For example, at 4:48 (Fig. 16a) the flow west of CL2 is generally from the south. However, just north of CL2 speeds increase and there is a more westerly component. This is consistent with observations of environmental air passing around a storm core and accelerating as it streams past (e.g., Browning 1984; Foote and Frank 1983). The enhanced westerlies above KHB 1 at 4:52 (Fig. 13c) are attributed to this flow around CL2.

At 4:52 (Fig. 16b), CL2 has started to decay; maximum upward motion now is only ~10 m s^{-1}. CL2 still exhibits a southwest–northeast orientation, but larger values of upward motion now intersect a greater portion of X5 than 4 min earlier (Figs. 16a,b; note the 2 m s^{-1} contour between 4:48 and 4:52). This corresponds to the expansion of UD in the east–west direction along X5 between 4:48 and 4:52 (Figs. 15b,c). CL2 intersects X5 over a relatively deep layer, as indicated by the vertical extent of UD in Fig. 15. A horizontal analysis of upward motion at ~900 m (not shown) indicates that the maximum near 900 m at 4:52 along X5 (i.e., near 80.695°W, Fig. 15c) also results from CL2.

Along X5 at 4:56 (Fig. 15d), the two regions of ascent (i.e., near 900 m, 80.69°W, and UD) continue above the sea air. However, the region near 900 m now extends to ~1.5 km. Note that UD is located farther east and above KHB 1+2 (Figs. 13d and 15d). In addition, maximum ascent in UD increases to over 4 m s^{-1} at 1.5 km (near 80.68°W). This also is evident in Fig. 16c. Specifically, UD clearly is seen near 28.46°N, 80.68°W (labeled UD, Fig. 16c; this region corresponds to UD in Fig. 15d). Farther south and west, the core of CL2 continues to decay (Fig. 16c). At 5:00 along X5 (Fig. 15e), UD continues to move eastward while remaining above KHB 1+2. Ascent now exceeds 6 m s^{-1} in UD. This also is seen in Fig. 16d (i.e., near 28.46°N, 80.675°W, labeled UD). It is in this region that CL4 begins to develop near 5:04.

It is important to determine why a storm develops in this region and not farther east or west. Therefore, the terms composing the vertical acceleration (1) were calculated at 2.5 km above the surface along X5 at 5:00 (just before storm development) (Fig. 17). ADV exhibits a minimum near 80.68°W and a maximum near 80.67°W (Fig. 17a, open circles). This is due to the upward motion associated with UD moving from west to east. Since the PGF force is slightly negative along X5 at 2.5 km (Fig. 17a, filled circles), it does not contribute to upward

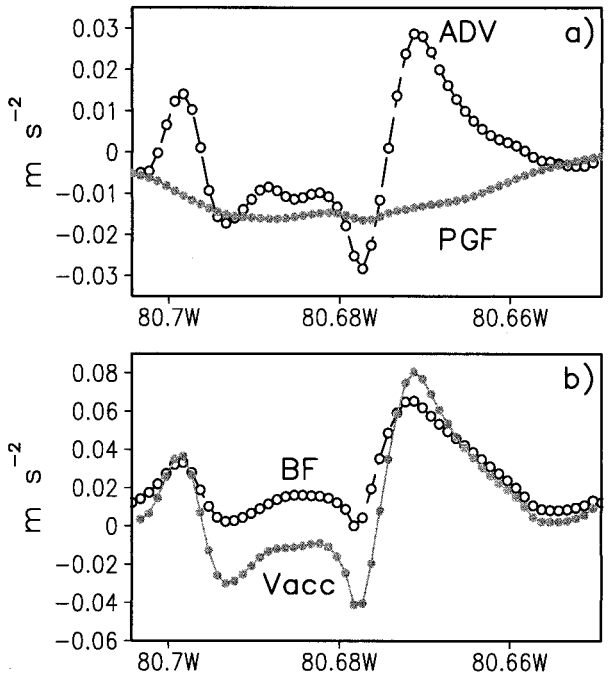

FIG. 17. (a) Three-dimensional ADV, PGF, and (b) BF and net vertical acceleration (Vacc) along X5 at 2.5 km above the surface at 5:00. All values are in m s^{-2}.

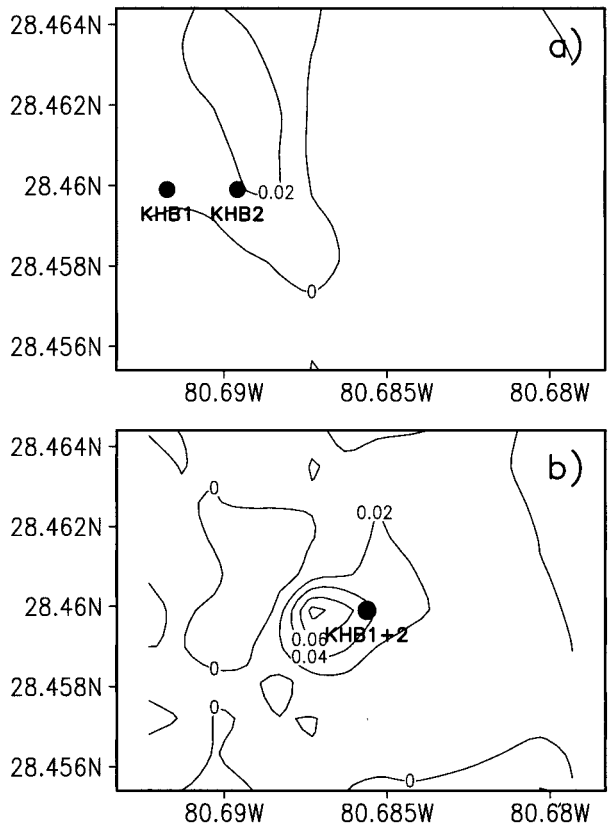

FIG. 18. Eastward advection of vertical momentum (m s^{-2}) at 700 m above the surface at (a) 4:52 and (b) 4:56. Dots indicate location of KHBs discussed in Fig. 13.

accelerations. The bottom panel reveals that BF is the dominant force acting to produce upward acceleration (Fig. 17b, open circles). Specifically, the buoyancy term is over twice as large as the advection term and is very similar to the total acceleration (Fig. 17b, filled circles, ~0.08 m s^{-2} near 80.67°W). This positive buoyancy is a result of a large thermal buoyancy acceleration in UD and is the primary factor in determining where along X5 the storm develops. The discussion above indicates that UD is a preferred region for storm development along X5. Therefore, it is important to determine why UD moved eastward and arrived at the location that CL4 initiated. That is investigated next.

One should note that UD exhibits little eastward movement between 4:48 and 4:52 (Figs. 15b,c), but then quickly moves eastward while intensifying between 4:52 and 4:56 (Figs. 15c,d). For this to occur, a source of displacement is necessary. Since OF3 is located south of UD at 4:56 (dotted line, Fig. 16c) it is not a factor. However, KHBs moving along the top of the SB interface are a possible source of displacement in this area. It is evident that UD is located above the strong circulation of KHB 1+2 at 4:56 (Fig. 15d). One should recall that KHB 1 and 2 merge into the larger and better-defined KHB 1+2 between 4:52 and 4:56 (Figs. 13c,d). This suggests that the resulting larger circulation (i.e., KHB 1+2) displaces the ascent already present above the sea air. The displacement of UD by the merging billows is evident in the eastward advection of vertical momentum (i.e., $-u\partial w/\partial z$, UADV) just above the billows (~700 m) at 4:52 (Fig. 18a) and 4:56 (Fig. 18b, dots indicate locations of KHBs in Fig. 13). At 4:52 (Fig. 18a) values of UADV reach ~0.02 m s^{-2} above the relatively weak and separate KHB 1 and 2 (near 28.46°N, 80.69°W). However, as KHB 1 and 2 merge into the more vigorous KHB 1+2, UADV becomes much greater (Fig. 18b, values ~0.08 m s^{-2}). This results from an increase in the u-wind component (due to the merging billows) followed by a stronger eastward advection of the upward momentum.

The above hypothesis is supported by noting that UD is located farther east at 5:00 (Fig. 15e) than 4 min earlier (Fig. 15d), while remaining above KHB 1+2. This indicates that UD continues to move eastward with KHB 1+2. Although values of upward motion in UD increase even further at 5:00 (i.e., ~6 m s^{-1}), part of that increase most likely is due to the closer proximity of OF3. Regardless, it is within this region that the updraft of CL4 develops (i.e., UD, Fig. 15f). These results indicate that the merging billows displace and intensify the region of ascent that was located above. However, critical to these conclusions is that the air within UD at 4:56 (i.e., just after the merger of the billows) originates from near the KHBs at the SB interface.

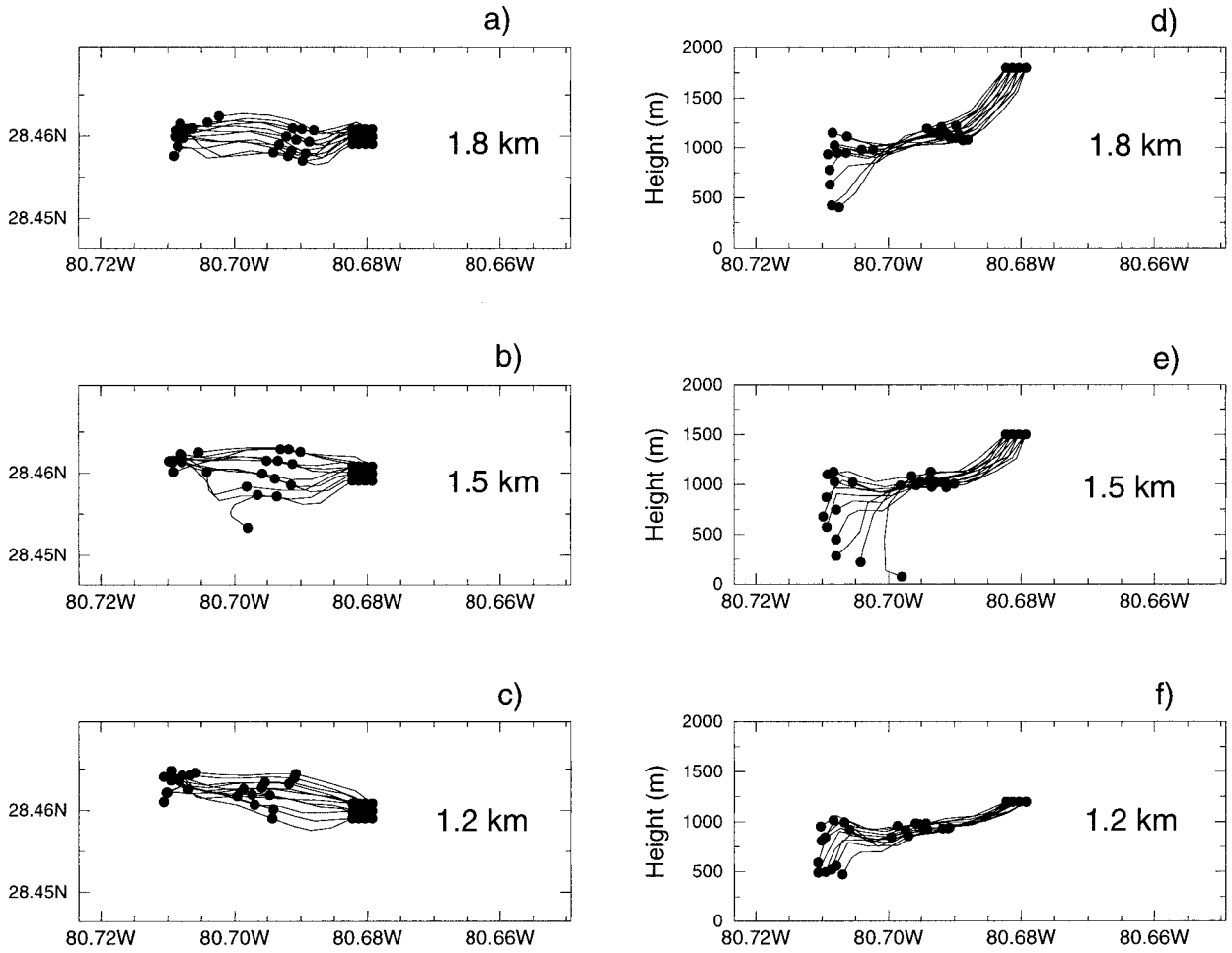

FIG. 19. (a)–(c) Horizontal and (d)–(f) vertical positions of backward trajectories arriving at 4:56 at clusters near (a),(d) 1.8 km, (b),(e) 1.5 km, and (c),(f) 1.2 km. Dots indicate locations at 4-min intervals.

We investigated whether air within the region of intensifying ascent originated from the KHBs along the SB interface by calculating backward air parcel trajectories. These trajectories describe the motions of air parcels over time and are useful for determining source regions. The kinematic method as described by Fuelberg et al. (1996) was used. The 4-min ARPS history data were linearly interpolated to a time step of 1 min in the computations. Since the goal was to determine the source of air above KHB 1+2 at 4:56, backward trajectories arriving at 4:56 at clusters near 1.2-, 1.5-, and 1.8-km altitude (i.e., within the region of enhanced upward motion) were calculated.

The dots in Fig. 19 correspond to trajectory locations at 4-min intervals. Specifically, dots on the right indicate arrival locations at 4:56, while dots in the middle (left) correspond to parcel locations at 4:52 (4:48). Results show that parcels arrive at the updraft from the west. Specifically, at 4:48 the parcels are located near 28.46°N, 80.71°W (Figs. 19a–c), which is just west of the SB front (see Fig. 8a). Their altitudes at 4:48 (Figs. 19d–f) indicate that the parcels originate at lower levels, that is, within the continental air west of the SB interface. Between 4:48 and 4:52, the parcels move over the SB front as they continue eastward. At 4:52 the parcels are close together both horizontally (i.e., within ~700 m, Figs. 19a–c) and vertically (i.e., near 1 km, Figs. 19d–f). This altitude is within the return flow above the SB interface. Between 4:52 and 4:56, the parcels continue moving eastward. These results indicate that air arriving in the updraft at 4:56 was at nearly the same altitude and horizontal location at 4:52.

The trajectories are related to the KHB circulations in Fig. 20. Specifically, the trajectory source region at 4:52 (labeled S, Fig. 20a) and arrival locations at 4:56 (labeled A, Fig. 20b) are superimposed on the *u*–*w* streamlines. It is important to note that the source region is just above KHB 1 and 2 at 4:52 (i.e., above the SB interface, Fig. 20a). This region is near the remnant of CL2 at 900 m that was discussed previously (Fig. 15c). These air parcels then are displaced upward and to the east, arriving above KHB 1+2 with larger upward mo-

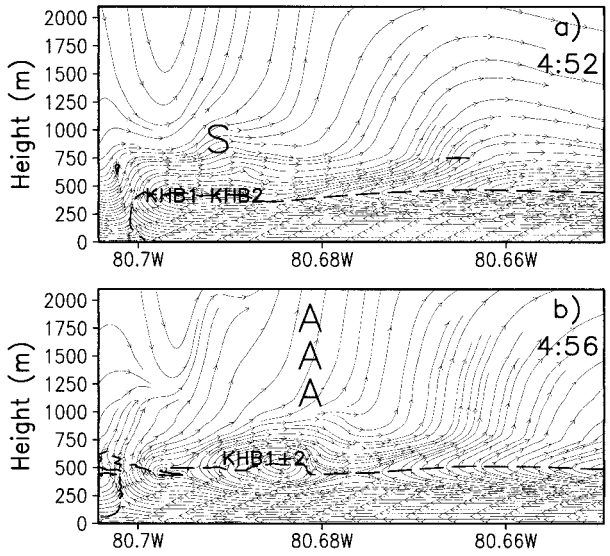

FIG. 20. (a) Trajectory source region at 4:52 and (b) arrival locations at 4:56. Point S denotes source region in (a), while A denotes arrival locations in (b). The *u*–*w* streamlines also are shown.

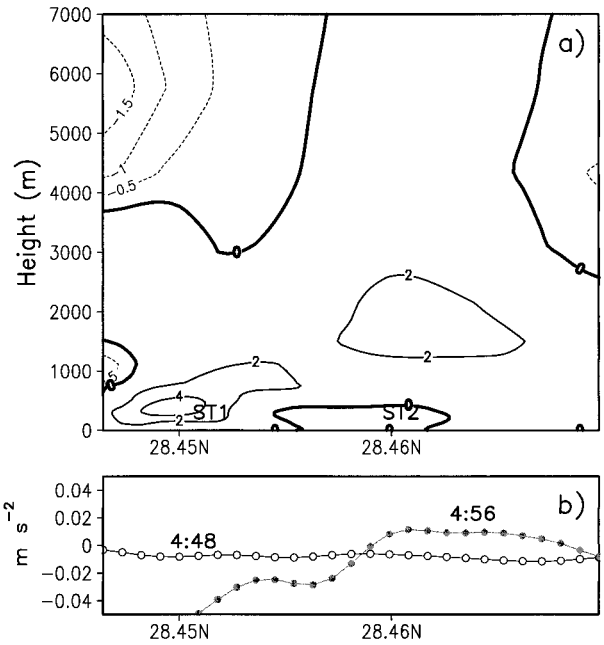

FIG. 21. (a) Cross section of the difference in vertical motion between 4:56 and 4:48 along X6 in Fig. 16d. Solid (dashed) lines indicate positive (negative) differences. Thick solid line denotes zero contour. Contour interval is 2 m s^{-1} (0.5 m s^{-1}) for positive (negative) values. ST1 and ST2 correspond to skew *T* locations in Fig. 22. (b) Total buoyancy force (m s^{-2}) along X6 at 4.3 km above the surface at 4:48 (open dots) and 4:56 (filled dots).

tion (i.e., UD in Fig. 15d) than before. The streamlines near the billows are consistent with this displacement. Thus, it appears that as KHB 1 and 2 merge into the larger circulation, the upward motion already present above the KHBs (i.e., the remnant of CL2, Fig. 15c) is enhanced and displaced eastward to higher altitudes. These results suggest that KHI aids in developing a preferred region for storm development along OF3.

The above discussion suggests why CL4 develops at the specific location along OF3; however, it does not explain the absence of storm development farther south (i.e., earlier) or farther north (i.e., later). To investigate this aspect, we prepared a cross section of the temporal difference in vertical motion between 4:48 and 4:56 (Fig. 21a, along X6 in Fig. 16d). Line X6 intersects the location where CL4 develops, and the times chosen reflect conditions prior to storm formation. (Recall that CL4 began to develop at ~28.46°N, 80.67°W near 5:04.) The region of increasing upward motion near the surface in the southern (left) area of the domain corresponds to OF3 motions (decreasing subsidence also would yield positive values; however, it only was present in small regions and does not alter our conclusions). Specifically, OF3 moves into the domain between 4:48 and 4:56. The increasing upward motion near 28.46°N at ~1.5 km corresponds to the intensification produced by KHB 1+2 discussed previously [i.e., UD near 80.68°W along X5 (Fig. 15c)]. The area of increasing upward motion extends higher than 7 km, consistent with Figs. 15b–d. The important feature is that both north and south of this increasing ascent the vertical motion above ~3 km shows increasing subsidence over the 8-min interval. Thus, as OF3 approaches the area from the south (the left), the region near 28.46°N provides the most favorable vertical motion for storm development.

This location can also be examined by noting the buoyancy force [term BF in (1)] along X6 at 4.3 km at 4:48 and 4:56 (Fig. 21b). At 4:48 (Fig. 21b, open dots) the weak negative buoyancy indicates general subsidence along X6. By 4:56 (Fig. 21b, filled dots) the buoyancy force in the southern region of the domain decreases substantially (i.e., become more negative), while values near 28.46°N (i.e., near the location of storm development) become positive (reaching ~0.02 m s^{-2}). Values north of the storm region remain slightly negative. The increased negative buoyancy to the south is a result of CL1. Specifically, at 4:48, CL1 and its associated subsidence are located southwest of X6. During the next 8 min CL1 drifts northeastward (note the region of upward motion near 28.44°N, 80.685°W in Fig. 16c that was not evident in Fig. 16a) producing subsidence that intersects the southern portion of X6. Thus, as OF3 propagates northward, this region of subsidence acts to suppress storm development. However, during this same period, the KHBs along X5 advect UD (and its associated upward buoyancy force) eastward (i.e., toward X6). It is apparent that this upward buoyancy force is able to overcome the negative buoyancy force that was present along X6 and create a favorable environment for convective development near 28.46°N. Thus, it appears that both the eastward movement of UD and sub-

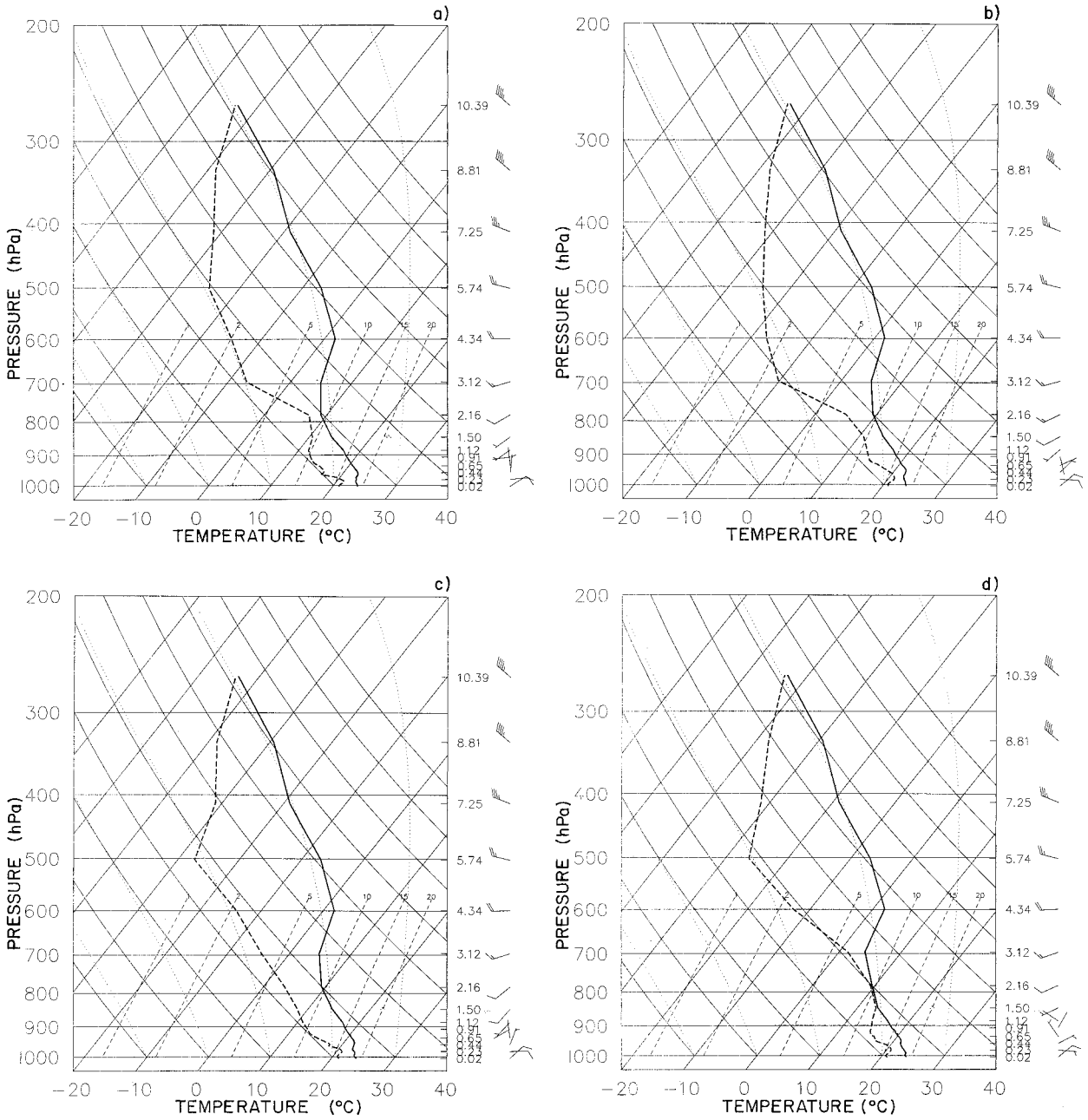

Fig. 22. Soundings at (a) ST1 at 4:48, (b) ST1 at 4:52, (c) ST2 at 4:48, and (d) ST2 at 4:56. Locations of ST1 and ST2 are shown in Fig. 21a.

sidence associated with CL1 aid in determining when CL4 develops.

The temporal trends in vertical motion that was just described affect the atmosphere's thermodynamic structure. This is indicated on skew T–log$p$ diagrams at two locations along X6 (denoted ST1 and ST2 in Fig. 21a). Storm development does not occur at ST1, and the soundings correspond to ~12 min (4:48) (Fig. 22a) and ~8 min (4:52) (Fig. 22b) before the arrival of OF3. In contrast, ST2 is located near the region of storm development. These soundings correspond to ~16 min (4:48) (Fig. 22c) and ~8 min (4:56) (Fig. 22d) before gust front passage. The times were chosen to exhibit the structure of the atmosphere at similar times well before gust front passage (i.e., 4:48) and at a consistent interval before its arrival (i.e., 8 min). The four profiles all reveal similar thermal structures throughout the depth of the atmosphere. However, the dewpoint profiles are different for each. Specifically, in the region of no storm development (ST1, Figs. 22a,b), the subsidence in the

middle troposphere dries the atmosphere between ~2.0 and 5.5 km. Dewpoints generally decrease ~1°C over the 4-min interval. In contrast, the region of storm development shows an increase in moisture between ~500 m and 5.5 km due to the upward motion that is transporting moisture to higher altitudes (Figs. 22c,d).

The effects of differential vertical moisture transport on atmospheric stability can be quantified using the *K* index (George 1960). The index is calculated as

$$K = T(850\text{ hPa}) + \text{Td}(850\text{ hPa}) - T(500\text{ hPa}) - \text{DD}(700\text{ hPa}), \quad (3)$$

where *T* is the temperature, Td is the dewpoint, and DD is the dewpoint depression. The *K* index is an indicator of potential instability, the availability of moisture in the lower levels, and the reduction of buoyancy through the entrainment of dry air. In general, the larger the *K* index, the greater the potential for storm development. The *K* index is a useful indicator of convective potential over Florida during the warm season (Fuelberg and Biggar 1994). The K index at ST1 decreases from 24 to 19 during the 4-min interval. Thus, the likelihood for thunderstorms is diminished by the drying associated with the upper-level subsidence. In contrast, the *K* index increases from 25 to 34 at ST2, indicating a reduction of stability and an increased chance for storm development. This indicates that the enhanced upward motion near 28.46°N creates a preferred location for storm development as OF3 moves toward the north.

In summary, KHI appears to help create a preferred area for storm development along an outflow boundary that is located behind the sea-breeze front. An area of upward motion above the sea breeze that was associated with a decaying storm was displaced by the KHI. A new storm developed within this region when surface lifting was provided (i.e., an outflow boundary). Regions surrounding the area of storm development exhibited negative buoyancy and no storms formed in those regions.

4. Summary and conclusions

The Advanced Regional Prediction System has been used to simulate land–water circulations and other small-scale features common to the Cape Canaveral area. The model was initialized with an inhomogeneous initial state and run in a two-way nested mode. Three nested grids with spacings of 1.6 km, 400 m, and 100 m were used.

The model was initialized with data from 4 June 1997. Storms formed along the sea-breeze front after it merged with the Indian River breeze and an outflow boundary. One of these storms produced an outflow boundary that moved northward. This outflow boundary produced a single precipitating storm behind the sea-breeze front. The cell formed when the outflow boundary intersected a deep layer of enhanced upward motion above the sea-breeze front. This region of upward motion initially was the remnant of a storm that formed along the sea-breeze front. However, before the cell completely decayed, a portion of its upward motion was enhanced and displaced by KHI that was located along the sea-breeze interface. This region of upward motion then moved along the updraft portion of the KHB. When the outflow boundary moved underneath this region of ascent, a storm developed. Thus, KHI aided in creating a preferred location along the outflow boundary for storm formation.

The region of enhanced ascent above the sea air also determined when the storm developed as the outflow boundary moved northward. Specifically, it was found that the region of ascent was limited to a relatively narrow, but deep, axis that was oriented in an east–west direction. Subsidence was present both north and south of this axis. Therefore, the thermodynamic structure was more favorable for storm development within the region of ascent than just north or just south. Thus, KHI helped create a preferred time for convective development during the lifetime of the outflow boundary.

In conclusion, the simulation presented here shows that KHI can aid in creating favorable conditions for convection on top of land–water circulations if additional lift is provided. Thus, the research describes a possible mechanism for producing storm development behind a sea-breeze front.

Acknowledgments. We would like to thank Dr. Kelvin K. Droegemeier of the University of Oklahoma for his many suggestions during this research. Dr. John Manobianco of the Applied Meteorology Unit at the Kennedy Space Center provided valuable insight into many modeling issues. Mr. Bill Roeder and the staff of the U.S. Air Force 45th Weather Squadron also have been extremely helpful. This research was supported by Subaward S96-75662 from the Cooperative Program for Operational Meteorology, Education, and Training (COMET) under a cooperative agreement between the Air Force Weather Agency (AFWA) and the University Corporation for Atmospheric Research (UCAR). The simulations were performed on the Environmental Computing Applications System Cray J90 at the Center for the Analysis and Prediction of Storms (Grant ATM91-20009 to the University of Oklahoma). The Cray J90 is supported by the University of Oklahoma, and by the National Science Foundation under Grant EAR95-12145 to Dr. Kelvin K. Droegemeier. The views expressed herein are those of the authors, and do not reflect the views of AFWA or UCAR.

REFERENCES

Arritt, R. W., 1993: Effects of the large-scale flow on characteristic features of the sea breeze. *J. Appl. Meteor.*, **32,** 116–125.

Asai, T., and I. Nakasuji, 1973: On the stability of ekman boundary layer flow with thermally unstable stratification. *J. Meteor. Soc. Japan,* **51,** 29–42.

Atkins, N. T., R. M. Wakimoto, and T. M. Weckwerth, 1995: Ob-

servations of the sea-breeze front during CaPE. Part II: Dual-Doppler and aircraft analysis. *Mon. Wea. Rev.*, **123,** 944–968.
Black, T. L., 1994: The new NMC mesoscale Eta model: Description and forecast examples. *Wea. Forecasting,* **9,** 265–278.
Blanchard, D. O., and R. E. Lopez, 1985: Spatial patterns of convection in south Florida. *Mon. Wea. Rev.,* **113,** 1282–1299.
Brewster, K., F. Carr, N. Lin, J. Straka, and J. Krause, 1994: A local analysis system for initializing real-time convective-scale models. Preprints, *10th Conf. on Numerical Weather Prediction,* Portland, OR, Amer. Meteor. Soc., 596–598.
Britter, R. E., and J. E. Simpson, 1978: Experiments on the dynamics of a gravity current head. *J. Fluid Mech.,* **88,** 223–240.
Browning, K. A., 1971: Structure of the atmosphere in the vicinity of large-amplitude Kelvin–Helmholtz billows. *Quart. J. Roy. Meteor. Soc.,* **97,** 283–299.
——, 1984: Morphology and classification of middle-latitude thunderstorms. *Thunderstorm Morphology and Dynamics,* E. Kessler, Ed., University of Oklahoma Press, 133–152.
Buckley, R. L., and R. J. Kurzeja, 1997: An observational and numerical study of the nocturnal sea breeze. Part I: Structure and circulation. *J. Appl. Meteor.,* **36,** 1577–1598.
Burpee, R. W., and L. N. Lahiff, 1984: Area-average rainfall variations on sea-breeze days in south Florida. *Mon. Wea. Rev.,* **112,** 520–534.
Byers, H. R., and H. R. Rodebush, 1948: Causes of thunderstorms of the Florida peninsula. *J. Meteor.,* **5,** 275–280.
Carpenter, R. L., Jr., K. K. Droegemeier, and A. M. Blyth, 1998: Entrainment and detrainment in numerically simulated cumulus congestus clouds. Part III: Parcel analysis. *J. Atmos. Sci.,* **55,** 3440–3455.
Christiansen, J., and N. Zabusky, 1973: Instability, coalescence, and fission of finite-area vortex structures. *J. Fluid Mech.,* **61,** 219–243.
Dailey, P. S., and R. G. Fovell, 1999: Numerical simulation of the interaction between the sea-breeze front and horizontal convective rolls. Part I: Offshore ambient flow. *Mon. Wea. Rev.,* **127,** 858–878.
Drazin, P. G., 1958: The stability of a shear layer in an unbounded heterogeneous inviscid fluid. *J. Fluid Mech.,* **4,** 214–224.
Droegemeier, K. K., and R. B. Wilhelmson, 1987: Numerical simulation of thunderstorm outflow dynamics. Part I: Outflow sensitivity experiments and turbulence dynamics. *J. Atmos. Sci.,* **44,** 1180–1210.
Estoque, M. A., 1962: The sea breeze as a function of the prevailing synoptic situation. *J. Atmos. Sci.,* **19,** 244–250.
Foote, G. B., and H. W. Frank, 1983: Case study of a hailstorm in Colorado. Part 3: Airflow from triple-Doppler measurements. *J. Atmos. Sci.,* **40,** 686–707.
Fuelberg, H. E., and D. G. Biggar, 1994: The preconvective environment of summer thunderstorms over the Florida panhandle. *Wea. Forecasting,* **9,** 316–326.
——, and Coauthors, 1996: TRACE-A trajectory intercomparison: Part 2. Isentropic and kinematic methods. *J. Geophys. Res.,* **101,** 23 927–23 939.
George, J. J., 1960: *Weather Forecasting for Aeronautics.* Academic Press, 637 pp.
Houze, R. A., Jr., 1993: *Cloud Dynamics.* Academic Press, 573 pp.
Lyons, W. A., R. L. Walko, M. E. Nicholls, R. A. Pielke, W. R. Cotton, C. S. Keen, and A. I. Watson, 1992: Observational and numerical modeling investigations of Florida thunderstorms generated by multiscale surface thermal forcing. Preprints, *Sixth Conf. on Mesoscale Processes,* Atlanta, GA, Amer. Meteor. Soc., 85–90.
Mahrer, Y., and M. Segal, 1985: On the effects of islands' geometry and size on inducing sea breeze circulation. *Mon. Wea. Rev.,* **113,** 170–174.
McWilliams, J. C., 1990: The vorticies of two-dimensional turbulence. *J. Fluid Mech.,* **219,** 361–385.
Miles, J. W., and L. N. Howard, 1964: Note on a heterogeneous shear flow. *J. Fluid Mech.,* **20,** 331–336.
Mueller, C. K., and R. E. Carbone, 1987: Dynamics of a thunderstorm outflow. *J. Atmos. Sci.,* **44,** 1879–1898.
Neumann, J., 1951: Land breezes and nocturnal thunderstorms. *J. Meteor.,* **8,** 60–67.
——, and Y. Mahrer, 1971: A theoretical study of the land and sea breeze circulation. *J. Atmos. Sci.,* **28,** 532–542.
Nicholls, M. E., R. A. Pielke, and W. R. Cotton, 1991: A two-dimensional numerical investigation of the interaction between sea breezes and deep convection over the Florida peninsula. *Mon. Wea. Rev.,* **119,** 298–323.
Nielsen, J. W., 1992: In situ observations and Kelvin–Helmholtz waves along a frontal inversion. *J. Atmos. Sci.,* **49,** 369–386.
Pielke, R. A., 1974: A three-dimensional numerical model of the sea breezes over south Florida. *Mon. Wea. Rev.,* **102,** 115–139.
——, A. Song, P. J. Michaels, W. A. Lyons, and R. W. Arritt, 1991: The predictability of sea-breeze generated thunderstorms. *Atmosfera,* **4,** 65–78.
Purdom, J. F. W., 1982: Subjective interpretation of geostationary satellite data for nowcasting. *Nowcasting,* K. Browning, Ed., Academic Press, 149–156.
Rao, P. A., H. E. Fuelberg, and K. K. Droegemeier, 1999: High resolution modeling of the Cape Canaveral area land–water circulations and associated features. *Mon. Wea. Rev.,* **127,** 1808–1821.
Sha, W., T. Kawamura, and H. Ueda, 1991: A numerical study on sea/land breezes as a gravity current: Kelvin–Helmholtz billows and inland penetration of the sea-breeze front. *J. Atmos. Sci.,* **48,** 1649–1665.
Simpson J. E., 1969: A comparison between laboratory and atmospheric density currents. *Quart. J. Roy. Meteor. Soc.,* **95,** 758–765.
——, 1994: *Sea Breeze and Local Wind.* Cambridge University Press, 234 pp.
——, and R. E. Britter, 1979: The dynamics of the head of a gravity current advancing over a horizontal surface. *J. Fluid Mech.,* **94,** 477–495.
——, D. A. Mansfield, and J. R. Milford, 1977: Inland penetration of sea-breeze fronts. *Quart. J. Roy. Meteor. Soc.,* **103,** 47–76.
Skamarock, W., and J. B. Klemp, 1993: Adaptive grid refinement for two-dimensional and three-dimensional nonhydrostatic atmospheric flow. *Mon. Wea. Rev.,* **121,** 788–804.
Taylor, G. I., 1931: Effect of variation of density on the stability of superposed streams of fluid. *Proc. Roy. Soc. London,* **132,** 499–523.
Trier, S. B., W. C. Skamarock, and M. A. Lemone, 1997: Structure and evolution of the 22 February 1993 TOGA COARE squall line: Organization mechanisms inferred from numerical simulations. *J. Atmos. Sci.,* **54,** 386–407.
Wakimoto, R. M., and N. T. Atkins, 1994: Observations of the sea-breeze front during CaPE: Part I: Single-doppler, satellite, and cloud photogrammetry analysis. *Mon. Wea. Rev.,* **122,** 1092–1114.
Wallace, J. M., and P. V. Hobbs, 1977: *Atmospheric Science: An Introductory Survey.* Academic Press, 467 pp.
Walsh, J. E., 1974: Sea breeze theory and applications. *J. Atmos. Sci.,* **31,** 2012–2026.
Weckwerth, T. M., and R. M. Wakimoto, 1992: The initiation and organization of convective cells atop a cold-air outflow boundary. *Mon. Wea. Rev.,* **120,** 2169–2187.
——, J. W. Wilson, and R. M. Wakimoto, 1996: Thermodynamic variability within the convective boundary layer due to horizontal convective rolls. *Mon. Wea. Rev.,* **124,** 769–784.
——, ——, ——, and N. A. Crook, 1997: Horizontal convective rolls: Determining the environmental conditions supporting their existence and characteristics. *Mon. Wea. Rev.,* **125,** 505–526.
Wilson, J. W., and W. E. Schreiber, 1986: Initiation of convective storms at radar-observed boundary-layer convergence lines.

Mon. Wea. Rev., **114,** 2516–2536.

Xian, Z., and R. A. Pielke, 1991: The effects of width of landmasses on the development of sea breezes. *J. Appl. Meteor.*, **30,** 1280–1304.

Xue, M., K. K. Droegemeier, V. Wong, A. Shapiro, and K. Brewster, 1995: ARPS version 4.0 user's guide. Center for Analysis and Prediction of Storms, University of Oklahoma, Norman, OK, 380 pp. [Available from Center for Analysis and Prediction of Storms, University of Oklahoma, 100 E. Boyd, Rm. 1110, Norman, OK 73019-1011.]

Zhong, S., and E. S. Takle, 1993: The effects of large-scale winds on the sea-land breeze circulations in an area of complex coastal heating. *J. Appl. Meteor.*, **32,** 1181–1195.

——, J. M. Leone Jr., and E. S. Takle, 1991: Interaction of the sea breeze with a river breeze in an area of complex coastal heating. *Bound.-Layer Meteor.*, **56,** 101–139.